*To my Parents,*

# Optimization of an analysis process of PET with PiB in Alzheimer's Disease

João Filipe Rodrigues Matos Lima

Supervisor: João Miguel Pereira

Dissertation presented to the Faculty of Sciences
and Technology of the University of Coimbra to
obtain a Master's degree in Biomedical Engineering

Physics Department

Faculty of Sciences and Technology of University of Coimbra

2013

# Acknowledgments

Eis que chega ao fim de uma das etapas mais importantes da minha vida e que marca para sempre, directa ou indirectamente, o meu futuro, pois com a apresentação deste documento concluo o meu percurso académico. Boas memórias ficam sempre associadas a todos estes anos de estudo, sendo que as mais recentes espelham os momentos passados na Universidade de Coimbra. Termino com esta tese o Mestrado Integrado em Engenharia Biomédica e chega então o momento de agradecer a todos aqueles que fizeram com que isto fosse possível, pois sem eles, todo este percurso encontraria obstáculos muito maiores do que aqueles que foram ultrapassados.

Em primeiro lugar, gostaria de agradecer ao Professor João Pereira pelo apoio incansável que sempre demonstrou e por toda a orientação prestada ao longo do desenvolvimento deste trabalho. O seu empenho e dedicação, bem como o seu conhecimento científico das matérias abordadas foram essenciais para que esta tese fosse elaborada com máximo rigor possível. Devo-lhe um agradecimento especial por ter demonstrado ser um orientador de projecto de mestrado exemplar, que sempre teve um papel activo em todos os momentos.

Ao Professor Miguel Patrício queria também endereçar um agradecimento devido a toda ajuda disponibilizada sempre que esta era solicitada. A sua opinião foi sempre oportuna quando surgiram dificuldades no projecto.

Todas as condições para o desenvolvimento da minha tese de mestrado foram as melhores que se poderiam desejar, quer no Instituto Biomédico de Investigação de Luz e Imagem da Faculdade de Medicina da Universidade de Coimbra, quer no Instituto de Ciências Nucleares Aplicadas à Saúde da Universidade de Coimbra. O fomento da investigação científica e a interdisciplinaridade transversal a estas duas instituições de investigação e ensino foi sem sombra de dúvidas essencial para que o meu trabalho fosse realizado com sucesso. A todos os responsáveis, nomeadamente ao Professor Miguel Castelo-Branco, Professor Antero Abrunhosa, Professor Francisco Alves e Professora Isabel Santana o meu especial agradecimento, pois o envolvimento destas pessoas foi fundamental para que os resultados obtidos fossem possíveis de alcançar.

Todo este percurso foi pautado com trocas de experiências e conhecimentos que de certa forma me ajudaram a crescer e a entender melhor o mundo à minha volta. Aqui, a Associação Académica de Coimbra, o Núcleo de Estudantes do Departamento de Física e a jeKnowledge

foram os principais meios de desenvolvimento de actividades extracurriculares, actividades estas que eu encaro como sendo essenciais no percurso académico de qualquer estudante. A todos aqueles com quem eu trabalhei nos diversos projectos desenvolvidos, o meu muito obrigado, pois convosco aprendi bastante, principalmente aqueles conteúdos que não estão disponíveis nas aulas e que apenas se obtêm através do trabalho em equipa e do envolvimento em novos desafios.

Muitas das experiências vividas foram com os amigos que sempre estiveram presentes nos bons e nos maus momentos. Alguns deles foram determinantes durante a minha passagem pela encantadora cidade de Coimbra: ao Flash, ao David, ao Pina, ao Gondomar, à Margarida, à Sara, ao Dani, ao Alzheimer, ao Pacífico, ao Pika e ao Morais, teço-vos um especial agradecimento pelo apoio constante, pelas trocas de opiniões, e essencialmente por personificarem aquilo que se descreve e se procura quando se pronuncia a palavra "amigo".

Faço também um agradecimento sentido à Marlisa pois demonstrou, com todo o seu amor, carinho e dedicação ser a melhor namorada que alguém pode desejar. Peço-lhe desculpa por todas as horas em que não me foi possível estar presente e quero-lhe agradecer pela motivação que me dava nas ocasiões em que eu precisava, e por todos os momentos felizes que passamos até agora. Sem ela, tudo seria mais difícil.

Por fim, chega a vez de agradecer às pessoas mais importantes da minha vida, aqueles que desde o início tornaram possível chegar onde cheguei. A minha família foi sem dúvida o meu pilar de sustentação. Ao meu irmão Luís, agradeço por me "abrir os olhos" quando era necessário. Embora não o expressasse da forma mais evidente, sempre foi um "irmão mais velho" preocupado e agradeço-lhe por isso. À minha irmã Cristina, agradeço por sempre me incentivar em tudo o que achava que era importante para mim e por utilizar a sua experiência de "irmã mais velha" para que me fosse mais fácil ultrapassar as barreiras que ela já tinha transposto no passado. Um obrigado por me passar toda a sua energia positiva. À minha Mãe, que sempre se preocupou com que nunca me faltasse nada desde o primeiro dia em que eu nasci, peço desculpa se por vezes a desiludi, e agradeço por tudo o que fez e ainda faz para que eu seja uma pessoa exemplar. Ao meu Pai, agradeço pelas palavras sábias e bons conselhos que sempre ditos nos momentos certos, ajudaram-me a formar a minha personalidade. Pai e Mãe, um Muito Obrigado por todo o esforço feito por vós na minha educação e para que me fosse possível tirar um curso superior. Sem vocês nada disto seria possível e por isso dedico-vos este trabalho.

# Abstract

Alzheimer's Disease is the most common cause of dementia in elderly people. Nonetheless, its diagnosis still presents some challenges, notably at the very early stage of the disease when the clinical presentation is not yet apparent: Such an early detection requires the use of molecular and genetic biomarkers. A key contribution to this comes from in vivo imaging using Positron Emisson Tomography (PET), as it allows for the detection of Aβ deposition and also for the monitoring of its progression. This is achieved by using the radiotracer Pittsburgh Compound B (PiB). The information extracted from the obtained scans requires a degree of processing in order to make it usable in a clinical setting. This thesis focuses on the development, optimisation and application of a processing pipeline for dynamic PET data to be used by clinicians, focusing on semi-parametric Standardized Uptake Values (SUV). This pipeline corrects for motion correction, accounts for space registration and motion, reference region normalisation, and extracts region of interest (ROI) data. This latter data is, however, hindered by the PET scanner limited spatial resolution leading to errors affecting the constructed images and distorting the true activity. This class of errors are known as Partial Volume Effects (PVEs) and are caused by the scanner Point Spread Function (PSF) and Tissue Fraction Effect (TFE): their correction is required to aid the correct interpretation of clinical PET data, both as a whole and through ROIs.. This thesis also focuses on the implementation and assessment of five different partial volume correction methods and the respective results are discussed in order to understand which one presents the best choice for general usage, to be integrated into the pipeline. This assessment also includes sensitivity-specificity analyses of PiB scans, as corrected by these methods, using an automated classifier. A continued investigation and improvement of PiB-PET analysis is therefore necessary to achieve better results in the future.

**Keywords:** Alzheimer's Disease, PET, PiB, SUV, PVC

# Resumo

A Doença de Alzheimer é a maior causa de demência nas pessoas idosas. No entanto, o seu diagnóstico ainda apresenta alguns desafios, nomeadamente nos estados mais precoces da doença quando o seu quadro clínico ainda não é evidente. Esta detecção precoce pressupõe o uso de biomarcadores genéticos e moleculares. Uma contribuição importante provém de imagiologia *in vivo* usando a Tomografia por Emissão de Positrões (PET), uma vez que esta tecnologia permite a detecção da acumulação da proteína Aβ e também a monitorização do avanço deste processo de acumulação. Isto é possível através do uso do radiotraçador Pittsburgh Compound B (PiB). A informação extraída dos scans obtidos requer um nível de processamento para que seja possível de ser usada em ambiente clínico. Esta tese foca-se no desenvolvimento, optimização e aplicação de uma pipeline de processamento de dados de PET, adquiridos com base num protocolo dinâmico, de forma a serem usados pelos neurologistas. As imagens são obtidas com base em Standardized Uptake Values (SUV). A pipeline tem em conta a correcção de movimento, o registo de imagem em diferentes espaços de referência, normalização à região de referência, e extrai também informação de cada região de interesse (ROI). Esta informação é, no entanto, afectada pela limitada resolução espacial do scanner PET, originando erros que influenciam a reconstrução das imagens e distorcem a actividade real. Este tipo de erros é conhecido por Efeitos de Volume Parcial (PVEs) e estes são causados pela Point Spread Function (PSF) do scanner e pelo Tissue Fraction Effect (TFE): as suas correcções são necessárias para proporcionar uma correcta interpretação da informação clínica das imagens PET, quer globalmente ou em cada ROI. Esta tese foca-se também na implementação e análise de cinco métodos diferentes de correcção de volume parcial (PVC) e os respectivos resultados são discutidos para se perceber qual dos métodos apresenta a melhor escolha para uso geral e para ser definitivamente integrado na pipeline. Este trabalho inclui também análises de sensibilidade e especificidade de scans PiB, corrigidas através destes métodos, usando um classificador automático. Uma contínua investigação e melhoria das análises de PiB-PET são portanto necessárias para alcançar melhores resultados no futuro.

**Palavras Chave:** Doença de Alzheimer, PET, PiB, SUV, PVC

# Index

# List of Figures

# List of Tables

# Acronyms

| | |
|---|---|
| AD | Alzheimer's Disease |
| Aβ | Amyloid-β |
| aMCI | Amnestic Mild Cognitive Impairmnt |
| BP | Binding Potential |
| CSF | Cerebrospinal Fluid |
| CT | Computed Tomography |
| DV | Distribution Volume |
| EM | Expectation Maximization |
| FDG-PET | Fluorodeoxyglucose-PET |
| FOV | Field of View |
| FWHM | Full Width at Half Maximum |
| GM | Grey Matter |
| GMM | Grey Matter Maps |
| GTM | Geometric Transfer Matrix |
| KeV | KiloElectronVolt |
| MCI | Mild Cognitive Impairment |
| MNI | Montreal Neurologic Institute |
| MG | Müller-Gartner |
| MRI | Magnetic Resonance Imaging |
| PET | Positron Emission Tomography |
| PiB | Pittsburgh Compound B |
| PSF | Point Spread Function |
| PVC | Partial Volume Correction |
| PVE | Partial Volume Effect |
| RF | Radiofrequency |
| RL | Richardson-Lucy |
| ROI | Region of Interest |
| RSF | Regional Spread Funtion |
| RVC | Reblurred Van Cittert |
| SUV | Standardized Uptake Value |
| SUVr | Standardized Uptake Value ratio |
| SVM | Support Vector Machine |
| TAC | Time-Activity Curve |
| TE | Echo Time |
| TFE | Tissue Fraction Effect |
| TR | Repetition Time |
| VC | Van Cittert |
| WM | White Matter |

# CHAPTER 1

## INTRODUCTION

Neurodegenerative diseases have a great impact in the quality of life of mainly the elderly people. Of these, the most predominant is Alzheimer's Disease (AD). In Portugal, around 153000 people suffer from any kind of dementia, 90000 of these are identified with diagnosed AD and according to Alzheimer Europe, the number of AD patients are approximately 7.3 million in Europe, estimating a duplication of these until 2040 in western Europe [1]. This thesis focuses on its impact in the human brain, notably on imaging diagnosis techniques, as well as on the respective processes of analysis.

Apart from its clinical presentation of progressive loss of episodic memory, AD may be characterized by the accumulation of plaques of Amyloid-β (Aβ) in certain regions of the brain, as well as by the presence of brain atrophy, notably in the mesial temporal lobe [2]. In order to test these *in vivo*, imaging techniques such as Positron Emisson Tomography (PET) and Magnetic Ressonance Imaging (MRI) are required: PET provides high signal sensitivity as well as the possibility of assessing measurements of the brain function; with MRI, this non-ionizing radiation imaging method provides good soft tissue contrast and high spatial resolution, making it ideal for analysing brain atrophy.

In this thesis, the focus will be in PET. Either Fluorodeoxyglucose (FGD) or Pittsburgh Compond B (PiB) can be used on AD investigations and diagnosis, but the main modality of this study was PiB-PET. PiB is a Carbon-11 radiotracer with 20 minutes half-life, which binds specifically to Aβ plaques. It was chosen as a focus of this study for two reasons. First, the production of PiB on Institute of Nuclear Sciences Applied to Health facilities together with the available PET scanner made possible the AD imaging with a predefined acquisition protocol. Second, the imaging processing and data analysis was performed in the Biomedical Institute of Investigation on Light and Imaging, in order to optimize a previous developed process of analysis of PET with PiB.

AD has different PET-PiB imaging profiles depending on the stage of disease, making it critical to assess the resulting scans in a systematic way. Here, the Standardized Uptake Value (SUV - Figure 1.1) assessed from the PET scanner plays a key role in the diagnosis, as it is a simple metric that can be compared among subjects. More refined, quantitative information can be obtained, through the calculation of parametric images of Binding Potential (BP) and Distribution Volume Ratio (DVR), but this work focus on semi-quantitative assessments, such as SUV and SUVr (Standardized Uptake Value Ratio), as these are enough for diagnostic purposes. In fact, a scan can be described as a table of mean SUVr values per region of interest (ROI), including both positive and negative controls, and these can help inform the diagnosis.

The use of ROIs in PET is limited by the quality of the images obtained. Looking in detail to the PET images below in Figure 1.1 it is noticeable the lack of anatomical detail, a characteristic of this imaging modality due to its low resolution (around 5mm isotropic) and large point spread function (PSF). As a consequence, PET images suffer from severe Partial Volume Effects (PVE). These effects can be described as the contamination of the areas with less uptake value because of the adjacent regions with higher radiotracer retention. This effect can be corrected with Partial Volume Correction (PVC) algorithms, one of the main themes in this thesis: PVC methods can provide finer detail, while making the mean ROI values more reliable. Several methods were applied providing different results either with images, values, or both. The results were compared and the some conclusions were made after the classification.

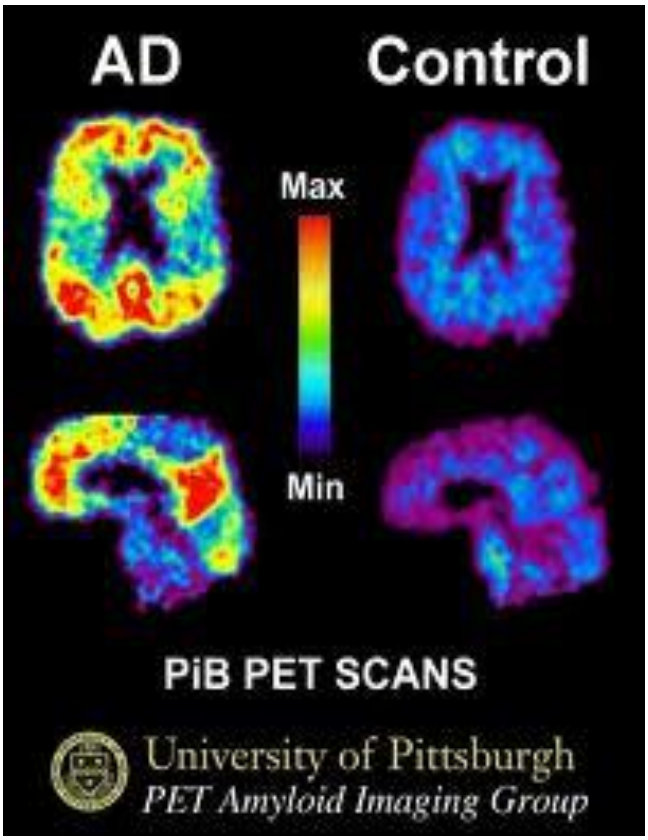


**Figure 1.1 - Comparison of SUV images from a control and an AD patients - University of Pittsburgh**

As a conclusion to this work, in order to explore the discriminating power of the PiB radioligand in diagnosing AD, an automated supervised classification (negative versus positive PiB scans) was performed through the use of a Support Vector Machine (SVM). This procedure also provided the necessary information to establish assumptions about which PVC method would be the more informative for solving this problem.

# CHAPTER 2

## STATE OF THE ART

## *2.1. Alzheimer's Disease*

The recent years have been presented with the strong efforts made on the study of neurodegenerative diseases by neuroscientists, physicist, psychologists and all the other professionals who are related to the field that studies the human behaviour and the mental illnesses. These kind of diseases do not allow the affected subject to notice when the biological development is beginning, and unfortunately most of the times it is their family or friends who verify slight differences in the social behaviour of the patients with an apparent loss of memory. Alzheimer's Disease (AD) is characterized by a slowly progressive disorder of the brain that leads to abnormal brain function and results in death [3].

Usually, the AD occurs after the 65 years of age. However, there are some cases of people who develop this condition in their 40s. The statistics show that 10% of people over the age of 65 may suffer from AD, but these numbers rise up to 50% if we refer to people around 85 years old [4]. It is important to underline that AD is not a normal condition of aging process, but by now, although science knows how to detect the disease and that it is not contagious, it is not totally clear how to avoid AD development. Since the beginning of all the investigations about AD, the significant differences in behaviour and psychological symptoms among patients are very difficult to understand, given that the physical changes in the brain are very similar from person to person. Typically AD evolves to a state of dementia characterized by the loss of mental skills and abilities including self-care capabilities, which are generally carried out by the family of the patients or by some other form of health care facilities [5].

According to the Alzheimer's Association and National Institute of Aging from USA, in 1984 AD was defined in one single stage and people without any symptoms were not assumed as suffering from the disease. This original definition comprises only the later stages of the usual definition that can be divided into three different phases: Preclinical AD, Mild Cognitive Impairment (MCI), and dementia caused by AD [6]. However, other research based in the criteria for the diagnosis of AD suggest a more complete and updated classification separating the whole process of AD into five stages [2]. The first indicator a possible or probable AD is the state of MCI. This state can be variably defined but most of the times the clinical condition includes subjective memory or cognitive symptoms or both, objective memory or cognitive impairment or both, and generally unaffected activities of daily living. Although this first stage is being classified as one indicator of AD, MCI presents a very wide meaning and it might be diagnosed in patients due to some other clinical reason rather than AD (eg.: fatigue, emotional or physical stress). The second indicator is the Amnestic Mild Cognitive Impairment (aMCI) and this can be described as

a more specific type of MCI in which there are subjective memory symptoms and objective memory impairment but the other cognitive processes remain normal as well as the daily activities. Again, the identification of this clinical situation might be synonym of dementia that is not AD. In a cohort of people with aMCI clinically identified to have progressed to dementia, just 70% met the neuropathological criteria for AD [2]. The period between the first brain lesions and the posterior appearance of symptoms is called Preclinical AD. Just the normal people that later fulfil the AD diagnostic criteria is classified as being in this stage. When the symptoms are clear but not severe enough to enter the criteria for AD the patients are categorized as being in the Prodromal AD phase, which is the predementia phase of AD, generally included in the MCI category. This is another wide concept that must be distinguished within the broad and different situations of abnormal cognitive functioning, typical from the normal ageing process. The last stage, when the symptoms are sufficiently severe to meet the clinical diagnostic criteria for AD, and the dementia is evident, the patients are classified as being in the stage of AD dementia. Although all the efforts are being done in order to detect AD or its first symptoms as soon as possible along the dementia development, a more refined and precise definition of AD is still needed to reliably identify the disease at its earliest stages [2].

Focusing on the diagnostic criteria used to distinguish the five stages described in the previous paragraph, it is also possible to identify the supportive features of these core criteria and the exclusion criteria. The alarm for a possible or probable patient with, or developing, AD is settled when there is noticed an early and significant episodic memory impairment over the last six months, with a gradual and progressive change in memory function. This symptom can be reported by the patients or by other people close to their. Usually the patients have also problems in recall and recognition testing and this does not improve significantly or does not normalize with cueing even though there was an effective encoding of the information before the onset of AD. The memory impairment can also be isolated or associated with other cognitive changes during the advance of the state of dementia [2]. The supportive features of these criteria are mostly achieved through imaging and according to other researches within the AD, the study of the biomarkers is today providing important knowledge about the state of dementia [7]. The Cerebrospinal Fluid (CSF) and Amyloid-β (Aβ) are specific biomarkers that can also provide information about the state of dementia [7]. A widely accepted assumption is that AD begins with an Aβ abnormal processing, more precisely, an irregularity on the processing of amyloid precursor protein, that leads to the formation of Aβ plaques and neurofibrillary tangles that results in abnormal protein depositions and characterizes AD pathologically, even when the patients are cognitively normal [7]. If the patients have low Aβ42 concentrations, or a positive

PiB Aβ imaging findings there is a great evidence of deposition of Aβ plaques. The correlation between these two facts is very high so these are valid biomarkers for the diagnosis support. The neurodegeneration may be assessed throughout the analysis of CSF-tau concentrations, Fluorodeoxyglucose-PET (FDG-PET) or structural Magnetic Resonance Imaging (MRI). The former is an indicator of possible pathological changes and associated neuronal injury. It can be divided in Total tau and Phosphotau and the concentrations of both increase when the patients are developing AD. CSF-tau is not specific for AD, however its higher concentrations are strongly associated with greater cognitive impairment and with the presence of neurofibrillary tangles in autopsy [7]. The brain metabolism is measured with the FDG-PET which includes a large indication about the synaptic activity. In the AD framework, decreased FDG uptake in the lateral temporal-parietal and posterior cingulate is typical in patients and the greater the decrease in the uptake of FDG-PET, the greater the cognitive impairment verified among the studied patients. There are also clear correlations between decreased FGD-PET uptake and both CSF Aβ and increased CSF tau, for cognitively normal elderly individuals, validating thereby FDG-PET as an indicator of the synaptic dysfunction that is present in neurodegeneration in AD [7]. The patients with symptoms that meet the AD diagnostic criteria generally show an atrophy of the medial temporal region with a volume loss of hippocampi, entorhinal cortex and amygdala. These evidences of cerebral atrophy, which is caused by dendritic pruning and loss of synapses and neurons, are possible to confirm with the Magnetic Resonance Imaging (MRI). Furthermore, there is a strong correlation between the severity of brain atrophy and the severity of cognitive impairment.

The biomarkers previously described have a fundamental role in the AD detection, having all of them different time-windows along the AD evolution, as can be expressed in Figure 2.1. The graph explains which biomarkers firstly provide valuable information about the stage of AD cascade. Figure 2.2 shows that the neurodegenerative biomarkers are temporally ordered and there is also an evidence that before the MRI changes, the neurologists might be capable of notice the FDG-PET changes suggesting that the brain metabolism start to become significantly different before any apparent sign of brain atrophy.

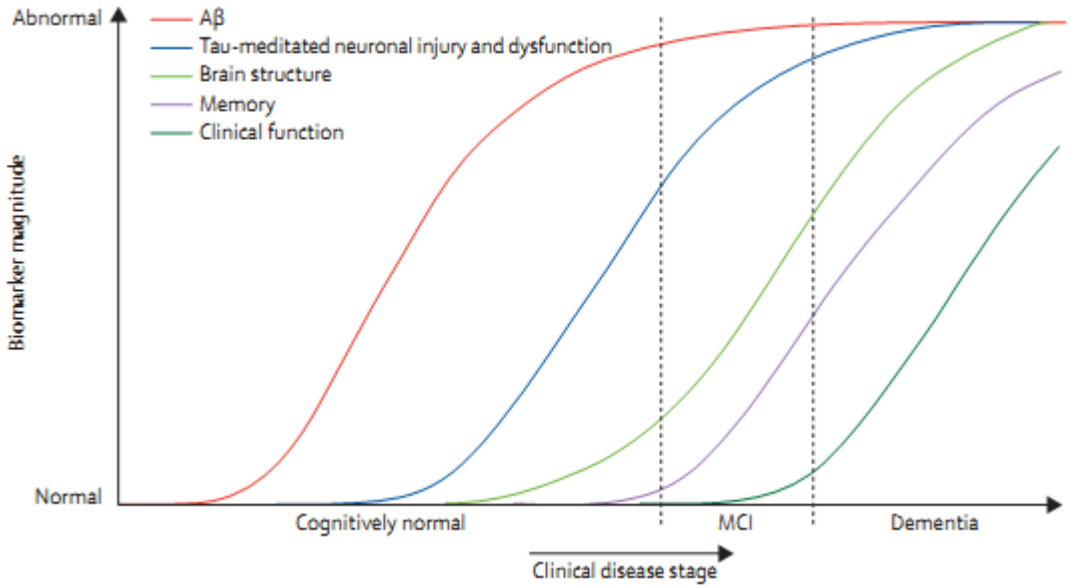


**Figure 2.1 - Dynamic biomarkers of the Alzheimer's pathological cascade. Aβ – Aβ42, Tau-mediated neuronal injury and dysfunction – CSF tau or FDG-PET, Brain structure – MRI.** [7]

The clinical disease stages are similarly correlated with the brain regions, i.e. at a given timepoint, different brain areas will be at different stages. Some regions might be firstly affected than other ones, and here imaging techniques play an important role because they can resolve the different phases of the disease both temporally and anatomically and this implies a great advantage of imaging biomarkers over fluid biomarkers. This statement can be confirmed by analysing Figure 2.2.

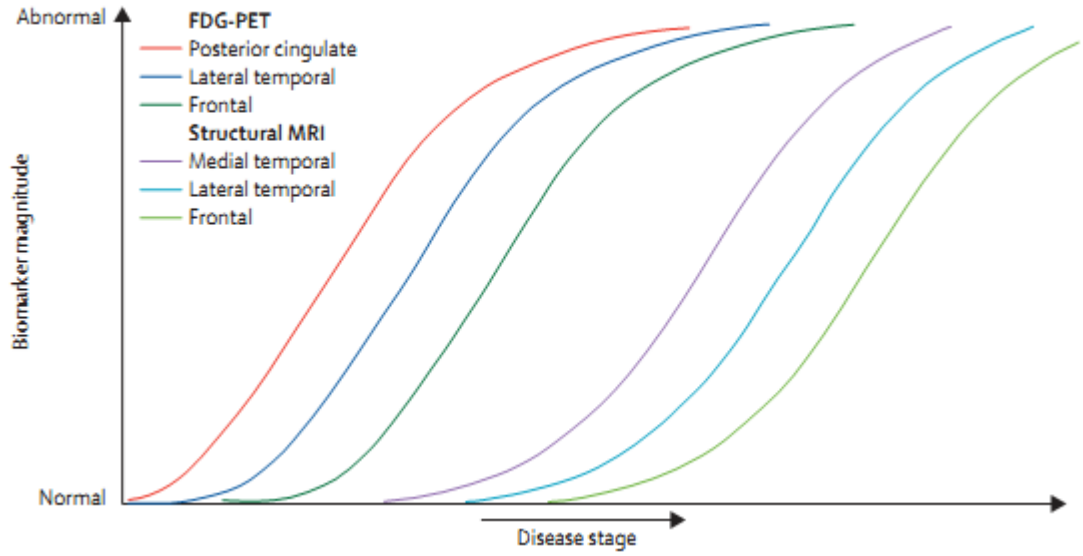


**Figure 2.2 – Anatomical imaging information vs Temporal Disease Stage** [7]

In the other hand, the exclusion criteria are also stated and it is possible to assure that there is a lower probability of an emerging AD in patients who accomplish these diagnostic criteria. First, if the patient has a sudden onset or if there is an early occurrence of gait disturbances or behavioural changes, it is too soon to assume that these are signs of AD. If the person has another type of dementia, some major depression, a cerebrovascular disease or even metabolic abnormalities which require specific investigations, the neurologists cannot identify a clear evidence of AD in these criteria. However, the clinicians should be sure that the patients are in the presence of definite AD when their have both clinical and histopathological indication of the disease, or if there is both clinical and genetic evidence of AD, with mutations on chromosome 1, 14 or 21 [2].

## *2.2. Imaging*

Along the imaging technology advances PET and MRI have been developed and provide different clinical advantages. On the one hand, PET enables measurements of biological metabolism using radioactive molecules. Due to its high sensivity – picomolar-range – PET is considered the modality of choice for molecular imaging. In the other hand, MRI modality offers a high spatial resolution with great soft tissue contrast. Also the fact of not using ionizing radiation is one more advantage of MRI. However, the poor spatial resolution of PET and the low signal sensivity of MRI are still problems to be solved in clinical imaging [8].

### 2.2.1. PET

PET was previously introduced as a key component of AD diagnosis. Entering into the detail of this modality, some essential parameters are needed to perform this analysis. First of all, it is necessary to define what is going to be analysed. Depending on the object of study, usually an abnormality of the physiology of certain organs, it is necessary to choose the proper radiotracer, a positron emitter. Looking in detail to the physics of the PET systems, during the natural decay of the radioactive molecule, the emitted positrons annihilate themselves with the free electrons, generating two antiparallel photons, both with 511 KeV. This split angle of 180° between the two produced photons makes possible the detection by the scanner of the exact position where the positron was emitted, and so, the 3D location of the radiotracer in the moment of that positron emission. The acquisition data is then processed with image reconstruction algorithms (not discussed herein) and consequent studies are made to analyse the biological outcome from the images. The process of data acquisition is explained in Figure 2.3.

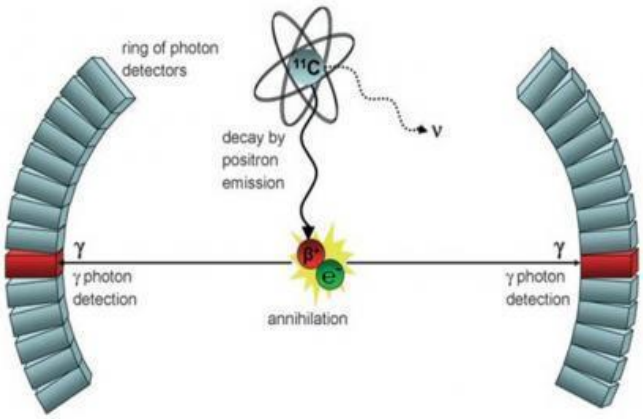


**Figure 2.3 - Scheme of PET physics and scanner performance** [9]

For AD diagnosis different radiotracers may be used, depending on what neurologists are analysing. In order to map and study the Aβ protein concentration or spatial distribution, PiB would be the best option to use due to its high affinity to this biomarker, as it will be explained on Section 2.3. On the other hand, if the aim of study is cerebral glucose metabolism to assess the possibility of the existence of some kind of neuronal injury, FDG-PET should be used [10]. However, the sensitivity and specificity of FDG-PET in AD is not as high as PiB-PET imaging in terms of biomarkers for MCI due to AD in MCI patients - Table 2.1 [10]. Sometimes abnormalities in FDG-PET scans might occur in cognitively normal patients who are at risk for future cognitive decline and aging is one factor that can modify this risk. Some authors suggest that if the degree of cognitive decline is uncertain, FDG-PET results might not provide clinical relevance in order to diagnose the state of dementia [11].

**Table 2.1 - Sensitivity and specificity for positive PiB-PET and FDG-PET biomarkers for MCI due to AD**

| Biomarker | Sensitivity | Specificity |
|---|---|---|
| Aged 50 - 89 | | |
| PiB-PET | 96.6% | 42.1% |
| FDG-PET | 93.3% | 23.6% |
| Aged ≥ 75, lower delayed recall | | |
| PiB-PET | 100% | 66.6% |
| FDG-PET | 91.6% | 44.4% |

Not only the Aβ accumulation in brain or the glucose metabolisms are measured in AD PET imaging. Neuroinflammation can also be assessed using [$^{11}$C]PK11195 which is a radiopharmaceutical that selectively binds to peripheral benzodiazepine present in the activated microglia. This cell is involved in inflammatory responses, and several studies have previously reported that brain inflammation is an active process underlying AD. Posterior cingulate, hippocampus and entorhinal cortex are brain areas where the radiotracer uptake is increased, in patients with AD. Although neuroinflammation imaging is still under evaluation, it was not part of this thesis framework [12].

Efforts are being made in order to develop new techniques that allow the diagnosis of early predementia states. As previously addressed on section 2.1 and graphically shown on Figure 2.1 and Figure 2.2, either PiB-PET or FDG-PET have the capability of identify earlier AD stages compared to structural MRI, that just evidences atrophy of the affected brain regions on prodromal stage [13]. The novel multimodal imaging techniques might have a relevant impact on the diagnosis of early predementia AD stages. In addition, the possible new approaches correlate PET with radiochemistry, that plays here an important role in the way of producing other radiopharmaceuticals which would made possible the imaging of neurotransmission in AD, such as cholinergic presynaptic terminals and glutamate synaptic function [12]. Regarding the various aspects of neurobiology of AD, PET provides valuable information, not only with PiB, but also using other radiotracers as described before. This imaging technique has several research applications which allow the neuroscientists to achieve an early detection and the efficient treatment monitoring, providing the better quality of life as possible to the patients [12].

### 2.2.2. MRI

MRI is a modality that is usually used in AD imaging due to its high spatial resolution and good soft tissue contrast. During the preclinical phase cognitively healthy elderly people may suffer from cognitive decline [2]. This phase can last for several years: the biological changes in the brain may start due to a clinically hidden pathology, eventually resulting in a visible presentation due to medial-temporal, including hippocampal, volume loss [13], [14]. The sooner the diagnosis of these typical brain changes and evidences of AD, the more efficient the treatment planning can be. MRI plays an important role in early detection based on brain anatomy changes.

The MR systems generate an external magnetic field that is felt by the nuclei in the body tissue, notably Hydrogen, the most common nucleus. The degree of magnetization is

proportional to the density of these nuclei, in other words, it depends on hydrogen concentration. This imaging modality is sensitive to these concentrations, and its efficiency in mapping soft tissues is higher when compared to X-ray imaging modalities such as Computed Tomography (CT). The imaging is possible due to the nuclei relaxation to their ground energy state after the magnetization. The usual relaxation processes T1 and T2 reflect the way the protons revert back to their resting states after the initial radiofrequency (RF) pulse provided by the MRI system. Each tissue has a unique T1 and T2 relaxation time. Usually the goal is to achieve a contrast image used to distinguish pathologic from normal tissue (not in AD imaging, though). The MR image contrast can be changed by performing alterations on the parameters of pulse sequences. The strength and timing of RF are specific on each pulse and the most important parameters are: the time between two consecutive 90° RF pulses, known as repetition time (TR) and the time between the initial 90° RF pulse and the echo, known as echo time (TE). T1 and T2 are related to these parameters. For T1-weighted sequences, the highest signal is obtained using short TR and TE (TR < 1 second, TE < 30 milliseconds). For T2-weighted sequences, by the opposite, long TR and long TE assure the highest signal (TR > 2 seconds, TE > 80 milliseconds) [15], [16]. For brain imaging the most used is T2-weighted sequences. Thus, the voxels will have an intensity that is related to the different relaxation times, which in turn depends on the characteristics of the tissue surrounding the nuclei, making this modality able to distinguish between e.g. grey matter and white matter in the brain [16]. This technique, however, has some disadvantages and not all the patients can be submitted to it. Metallic objects must be taken out of the room where the machine is operating, people with pacemakers cannot be scanned due to the high magnetic fields generated and the patients that suffer from claustrophobia should be advised and conscious about the tight space where they have to be during the exam. The necessity of holding very quietly during a long period of time and the very loud noise produced by the machine are also some other disadvantages of this imaging technique [17].

As explained previously, as AD progresses, the brain morphology suffers changes that are possible to see in MRI. Figure 2.4 shows a coronal slice of a MRI scan performed in a normal subject, as well as in two other subjects in different stages of the disease: a mild cognitive impairment (MCI) stage, which can be considered pre-AD, and an advanced case of AD. The differences in brain morphology are clear, as is the progression of the atrophy, mostly affecting the hippocampi and surrounding tissue, the posterior cingulate, and enlarging the ventricles in the process.

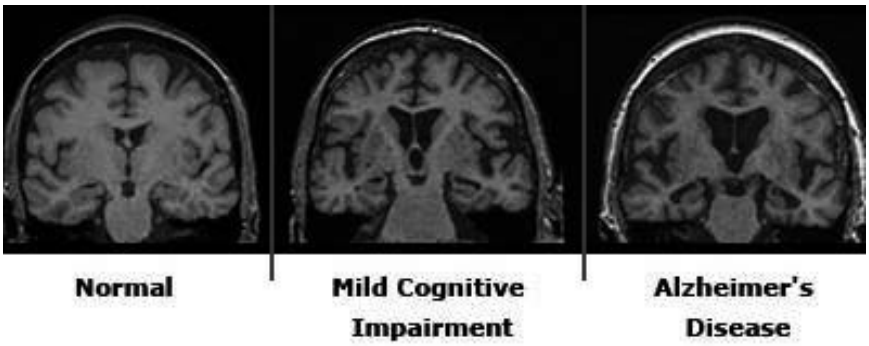


**Figure 2.4 - Differences in brain morphology in different stages of AD comparing to a normal subject** [18]

## *2.3. Pittsburgh Compound B*

It was 100 years ago when Aβ plaques and neurofibrillary tangles were recognized as the neuropathological hallmarks of AD and on that period, its presence or absence could only be assessed post-mortem using the available techniques such as dyes that identified such structures microscopically [19]. Molecular imaging has upgraded our knowledge of the time course of biological events leading to AD. Amyloid imaging has shown high accumulation of amyloid in very early state of disease and precedes functional changes measured as reduction in cerebral glucose metabolism and cognitive impairment as already explained before [20]. After a decade of investigation studies and evaluations to improve the first PiB molecule ([$^{11}$C] N-methyl [$^{11}$C] 2-(4'methylaminophenyl)-6-hydroxy-benzothiazole), involving chemical modifications and design improvements, the first successful Aβ plaques-specific PET imaging study was achieved in a patient clinically classified as probable AD. This molecule, which is an analogue of Thioflavin-T, was chemically labelled with positron emitter 11-Carbon ($^{11}$C) and nowadays, ten years after this first study, PiB remains as the most used radiotracer in many human research protocols throughout the world to detect early AD due to its high affinity and selectively binding to only fibrillar forms of Aβ, demonstrating its usefulness many years before the clinical diagnosis of AD [19].

In order to validate PiB and its suggested features, patients had to undergo conventional PET imaging to determine the brain areas that showed lower levels of brain activity (FDG-PET). After this, the same patients were again submitted to PET imaging but with PiB, to see if the areas which had shown low brain activity met the areas with Aβ accumulation. To evaluate the amounts of PiB that were bounding to amyloid, sequences of blood samples were taken from each patient during the imaging. The samples were analysed and provided a comparison between

the amounts of PiB entering and leaving the brain. Through these measures it was possible to confirm the specific binding of PiB to Aβ [21].

A typical study for fully quantitative PiB PET that included MRI scan, arterial input function determination and 90 minutes of PET data acquisition is described in [22]. 15 patients have been undergone to this study (5 AD's, 5 MCI and 5 controls) and verified that the level and pattern of Standardized Uptake Value (SUV) measures were consistent with those observed for the quantitative PiB retention measures (which are going to be described later on) and showed significant differences in the magnitude and distribution of PiB binding measures in AD subjects compared with controls. The results of this study showed that MCI subjects were classified as having either control-like or AD-like patterns of PiB retention.

Recently (approximately 6 year ago) a newer and longer-lived Aβ specific binding radiotracer has started to be developed. $^{18}$F-florbetapir was already approved for clinical use and its great advantage comparing to PiB is the half-life. The use of PiB is only possible on facilities which have cyclotron due to its ~20 minutes half-life. More and more exams are needed until the usage of florbetapir reaches the levels of PiB usage [19]. Its unambiguous interpretation of the specific binding in human brain is the key factor for using PiB for early disease detection. The wide scientific knowledge about this radiotracer is also a proof of confidence for its usage, although the comparisons that have already been made suggest high correlation between both radiotracers [23].

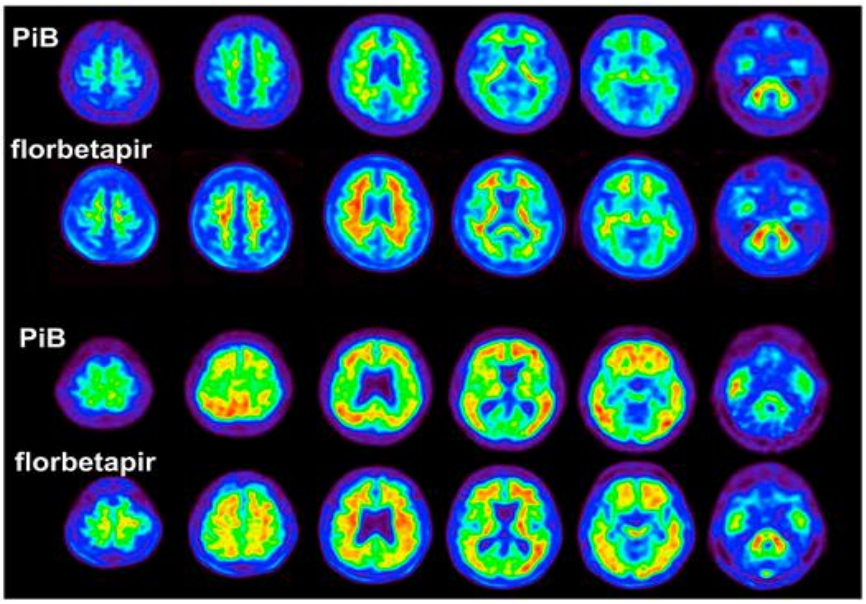


**Figure 2.5 - Axial slices of florbetapir and PiB scans of two subjects. A cognitively normal control on the top showing low radiotracer retention and an AD patient on the bottom with high radiotracer retention (SUVr)** [23]

Some region based studies were performed with PiB for AD purposes [24], [25]. Among all the analysed regions, frontal cortex showed higher PiB uptake in AD subjects, comparing with the other regions, but occipital, parietal and temporal cortex as well as striatum have also shown increases in the radiotracer uptake levels. Other regions such as cerebellum, pons and subcortical white matter were confirmed as having similar levels of binding places for PiB across all the subjects (AD, MCI and controls) [24].

The existence of regions with such characteristics presented above (non-specific binding) is extremely useful in SUVr analysis as it will be explained on sections 3.2 and 3.3. In the case of PiB, cerebellum was chosen as the reference region to be used, since it always shows a lack of fibrillar amyloid plaques [24]. In order to support this statement, in a post-mortem analysis negligible levels of binding PiB to cerebellar grey matter were found either in AD subjects, controls, and also non-demented AD subjects [22]. Thus, to perform the SUVr calculation the obtained values from the different regions are normalized to the ones obtained in the reference region, minimizing therefore the influence of nonspecific effects.

# CHAPTER 3

## CARACTERIZATION OF PIB-PET SCANS

Regarding the use of PiB on PET studies, there are two main approaches that can be performed in order to yield the proper conclusions about the activity distribution over the analysed regions. These approaches can be divided into quantitative methods and the semi-quantitative methods. The objective of the next sections is to describe and compare both methods with the perspective that semi quantitative methods may be a strong alternative to quantitative methods, providing results with similar clinical relevance and with lower complexity of implementation and analysis.

The former are based on compartmental models, which allow the radiotracer quantification on the different regions depending on its specific binding. The regions are described as compartments and the radiotracer kinetics within this system are explained with a mathematical framework based on differential equations [22], [26], [27], [28]. Semi-quantitative methods use the standardized uptake value (SUV) provided by the PET scanner to analyse the tracer distribution over the brain of the patients, through images, where the regions with higher uptake are emphasized according to a colour scale. Usually reference regions are used to obtain SUVr (relative SUV) images, usually the ones analysed by the neurologists [22], [29].

The basis of both methods will be explained on the following sections, giving more attention to the semi-quantitative methods which were the main focus of this thesis, regarding the methodology for PiB data analyses.

## *3.1. Quantitative Methods*

Quantitative methods are based on mathematical formulations used to understand the tracer kinetics within the biological system, notably the way the radiotracer flows and specifically binds in the brain. A common formulation relies on the use of compartmental models [27], the choice of which depends on the chemical and biological properties of the radiotracer [27]. The aim of these methods is to achieve a valid quantification of certain parameters [30], required for a proper quantification of the PET data in a so called parametric fashion, i.e. the images are fully quantitative in their information, the value at each coordinate corresponding to a certain biological parameter [22].

A general compartmental model is shown in Figure 3.1, as well as the respective parameters describing how the radiotracer concentration on each compartment influences its binding and its dynamics over the compartments. Arterial blood is assumed as the first compartment, on the left. The radiotracer flows from arterial blood to the free compartment, and the other way around, according to the transfer rate of $K_1$ and $k_2$, respectively. The exchange between the free

compartment, where the tracer is in the brain tissue but unbound, and the binding compartment, where the tracer is specifically bound to the structures that are likely to be detected, is described by the rate constants $k_3$ and $k_4$. The non-specific binding compartment, is also included [27], [30].

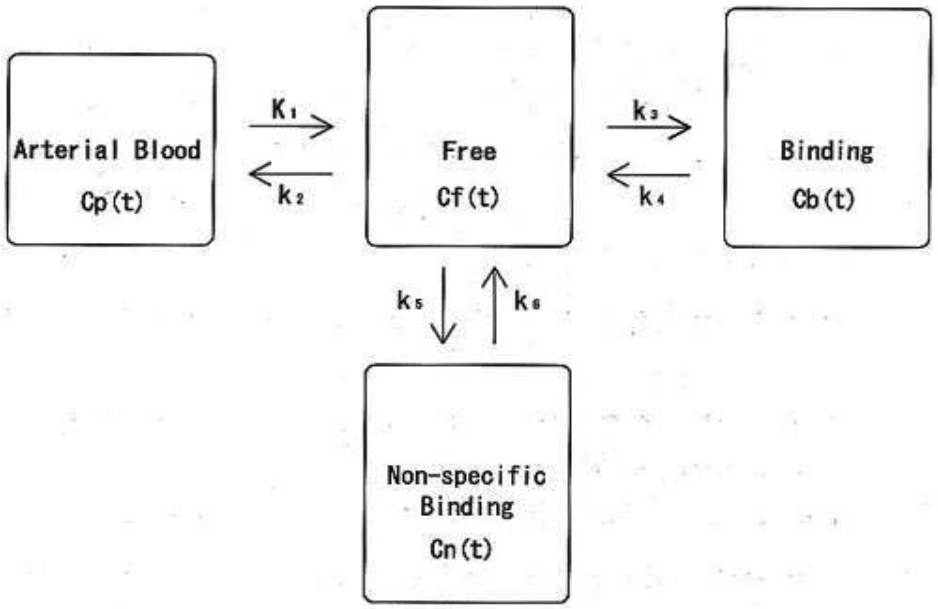


**Figure 3.1 - Three tissue compartmental model** [27]

Usually, on quantitative studies, the most relevant parameters that can be achieved are the distribution volume (DV) and the binding potential (BP), which detailed formulations are not going to be addressed here. Assessing these macro parameters provides important information either about the radiotracer dynamics such as its pharmacokinetics and/or about the physiological function, which can be very useful to perform a precise diagnosis [27].

As said before, the number of compartments used in the model depends on the chemical and biological properties of the radiotracer which is going to be studied. For instance, using the model presented on Figure 3.1, most of times it is difficult to estimate with precision the six parameters at once due to the statistical quality of the PET data [27]. This wide statistical variability of parameters can be decreased or even suppressed by reducing the number of compartments in the model. The radiotracer addressed on this work is PiB and its dynamics in human body can be analysed using the two tissue compartmental model [31], described by only 4 rate constants - Figure 3.2. The rapid equilibrium between the non-specific binding and free compartments allows the removal of one compartment thus, this model is enough to interpret the tracer kinetics [27].

However, these methods require the precise quantification of arterial input function, generally obtained by an invasive procedure such as arterial cannulation where blood samplings are collected during the acquisition protocol [30]. These techniques are troublesome and in order to avoid the invasiveness and the complexity of scanning protocol, the arterial input function given by blood sampling can be replaced by using a reference region model. These are preferred to the ones that require the blood sampling and are used when a suitable reference region is available [28]. Usually the chosen reference region is the one which best describes the radiotracer non-specific binding and in the case of PiB it is grey matter cerebellum.

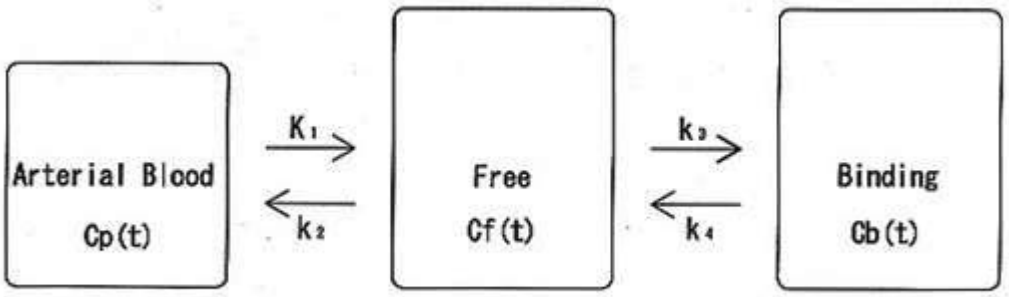


**Figure 3.2 - Two tissue compartmental model** [27]

In addition, using the reference region models through either the Logan graphical analysis [28], the Lammertsma simplified reference tissue model (SRTM) [30] or the Gunn receptor parametric mapping (RPM) [26] frequently leads to inaccurate estimation of arterial blood concentration assuming that all the pixels of interest within the PET scanner field of view (FOV) share the same arterial input function [27]. These assumptions require care when performed, and the use of semi-quantitative methods may present an alternative technique to the quantitative analysis.

## *3.2. Semi-Quantitative Methods*

As an alternative to the previous quantification methods, the use of SUV is a different way of assessing the physiological function through images without being necessary the use of blood sampling [29], while also avoiding complex mathematical operations, fairly approximated in the absence of arterial blood samples. The use of quantitative methods is still fundamental within a research setting, given the mathematical properties of the resulting images, but a cruder approach is acceptable in a clinical context, where the analyses of scans are performed visually most of the time.

SUV has been widely used in PET imaging and in the recent years, and studies have been performed in order to compare both quantitative and semi-quantitative methods in PET in order to establish a correlation between them, and to assign the comparable clinical relevance to both methods [22]. SUV is a unitless measure and is calculated:

$$SUV(t) = \frac{c(t)}{injected\ dose/body\ weight} \qquad \textbf{Equation 3.1}$$

having $c(t)$ as the tissue radioactivity concentration at time $t$ (Bq/Kg), the injected dose $c(t = 0)$ (Bq) and the patient body weight (Kg) [32].

An important reason for using this method in PET is that SUV images, contrary to raw PET data that depends on the injected dose and patient volume, are easily comparable amongst different subjects, notably when trying to distinguish controls from patients [33]. There are additional factors affecting SUV, such as the body composition and the length of the acquisition protocol. The variability on SUV because of the body composition is often related to the percentage of fat in the body. For instance, in the case of FDG, fat has much lower uptake comparing to other tissue. Corrections regarding this effect have already been proposed [34] and will not be further discussed, as this is not an issue in PiB. The length of acquisition affects the SUV in the way that the radiotracer has different dynamics in the course of the time. In the case of PiB-PET, studies were performed searching for an optimal time-window to use on SUV measurements (40-70 minutes) and the best results of SUVr analysis are achieved when the proper protocols are used [22], [29]. Partial volume effects have also an impact on the quality of the images obtained with this imaging modality [35]. These effects are related to the nature of PET systems and to image reconstruction algorithms. This topic will be addressed on the following chapters.

In order to account for further inter-individual variability, SUVr images are used due to their improved reliability and low test-retest variation [29]. SUVr represents the ratio between the SUV values of the brain and the SUV values of the reference region. The reference region is chosen so that it does not show uptake variation between confirmed patients and controls [22], [29]. In order to perform this normalisation, the acquisition interval is not irrelevant. Concerning AD PiB-PET analysis the most used time-window for obtain the relevant SUV measures is the one referred in the above paragraph (40-70min) [22], [29]. The ROIs and the frequent reference region used for SUVr have also been aim of study in some comparisons [22] which will be explained in the next section.

## *3.3. Comparison between quantitative and semi-quantitative methods in AD PiB-PET studies*

The most common outcome measures of quantitative methods on PiB-PET studies are frequently the DVR and BP [22]. Both DVR and BP are directly related to the availability of binding-sites in a certain region of interest. As the concentration of the specific regions cannot be measured but only the total tissue concentration [30], considering the compartmental model, a suitable reference region has to be used.

Although the focus of this thesis relies on SUVr analysis, the main comparisons between quantitative and semi-quantitative methods were studied. Those have been supported by region based analysis and the key evaluations were performed to DVR and SUVr [22], [29]. These investigations were made in order to assure that SUVR analysis could easily provide clinical results similar to the ones given by DVR, with less complications. Different time intervals and several ROIs (a few more ROIs than the ones addressed on section 2.3) were used on both the experiences that support these comparisons [22], [29]. The main aims of this studies were the evaluation of the correlation between the Logan graphical analysis and SUVr, and the contrast of SUVr between AD patients and controls [29].

On one study [29], the first evaluation focus on comparing SUVr to DVR for each time window, each individual ROI and across AD, MCI and control subjects. The achieved results showed a great correlation between SUVr and DVR with slight variations depending on the time-window. This correlation was higher for the latest time windows when using the arterial input function and for the intermediate time windows (40-60 and 40-70min) when using cerebellar reference region [29]. The differences between SUVr and DVR using cerebellar reference region were slight and identical across the analysed ROIs.

The second evaluation focused on the effect that each ROI had on differentiating AD from control subjects. This assessment was made throughout the predefined time-windows, taking into account the simple group mean difference and the effective contrast for each ROI. The results showed that the greatest differences in group means were verified on Pregenual Anterior Cingulate, Dorsal Frontal Cortex and Anterior Ventral Striatum [29]. In contrast, the ROIs that did not show a significant difference or even negative difference were Pons and Mesial Temporal Cortex.

The last assessment on this study was the evaluation of SUVr temporal dynamics between AD and controls. The PiB uptake and DVRs were simulated using the arterial input function obtained from the two-tissue compartmental model. As expected, the PiB uptake was higher for

AD than for control subjects over the acquisition period and the dynamically changing of SUVr suggested that it might be unstable at earlier times [29].

From all the experiments performed over this study, the researchers conclude that it is simple to reach a great proximity between SUVr and DVR. They also verified that SUVr overestimated DVR and the degree of overestimation increased for later time-windows. Thus, taking into account the measurements stability, study feasibility and outcome similarities, they suggested 40-70min as the optimal time interval for SUV measures regarding PiB-PET analysis in AD.

On the scope of the comparisons between quantitative and semi-quantitative methods, another work [22] was carried out with a different methodology than the comparison described before. The aim of these experiments was to extend the quantitative PiB studies to include an evaluation of simplified methods of analysis, such as SUVr [22]. Similarly to the previous one, this study underwent experiences with and without blood sampling. The data analysis was based on 3 different outcomes and two time windows (60min and 90min): the results obtained from SUVr using cerebellum as reference region; the Logan graphical analysis in order to assess PiB specific retention through DVR calculation, using arterial input function from blood sampling and from Carotid imaging; the Lammertsma SRTM image-based analysis to study the radiotracer dynamics and to obtain BP.

The results showed that 90min analysis achieved better results than the 60min one, although this also yielded useful data. The estimation of input function from carotid imaging showed important limitations mainly on assessing the unchanged fraction of PiB on plasma, which resulted on overestimations of DV values. However, these results were comparable to the ones that were achieved by using the arterial input function, in terms of test-retest variation. The use of a reference region for input function determination appears to be more stable than either blood samplings or carotid imaging methods. Regarding the analysis simplification, SUV is most used in clinical studies where input function determination is not required. For PiB data, SUVr values were relatively constant for an analysis of 40min after the tracer injection in both AD and controls. The use of this ratio is also useful since it eliminated some sources of variability on calculations, such as the body composition. In addition, cerebellar imaging must be carefully assessed due to the possible artifacts that may appear such as cerebellum region misplacement and PiB measurements contamination from adjacent regions. Taking into account the whole achievements of this study, the researchers concluded that 90min SUVr analysis shall be the method of choice when the simplicity of calculations is the main concern, presenting a valid alternative to quantitative arterial based methods.

## *3.4. Using Support Vector Machines for imaging classification*

Machine learning plays an important role on computed techniques for automatic classification of imaging scans [36]. The classification procedures are based on pattern recognition which is related to the discovery of regularities among datasets which leads the computed algorithm to the organization of the data into different categories [37]. In order to perform this classification, the algorithm needs to extract the features that are going to be used to compare the data. These features are just data characteristics able to be compared across the all dataset. After choosing the features, a proper feature selection has to be done to create a suitable learning model. This selection can improve the algorithm performance by removing all the irrelevant features and thus the whole process become faster and more precise [37]. For instance, in the case of AD vs controls classification, a feature selection would select just the ROIs that are known as having specific binding levels of PiB comparing to controls, such as posterior cingulate, frontal cortex and precuneus. After these procedures, the algorithm is trained with previously labelled data, and use the information gathered during the training to classify the unknown datasets according to the classification used in the training processes. The general performance of a classification algorithm is described below on Figure 3.3.

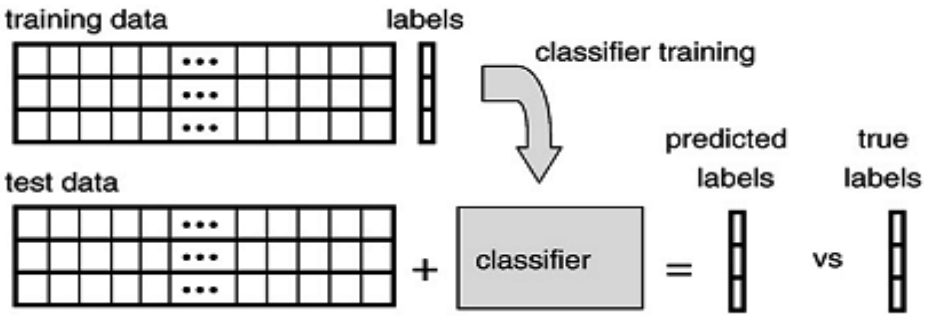


**Figure 3.3 – Performance of classification algorithms [38]**

On this work, the classification was used to classify the scan as AD or non-AD so the used labels were just two. Furthermore, the used algorithm was the Support Vector Machines (SVMs). For binary classification, SVMs searches for the optimal solution for the classification of subjects according to pre-defined criterion. The optimal solution is the highest distance that can separate two subjects from different classes [36]. The classified subjects can be expressed as points in a 2 dimensional plot and the separating line between the groups is known as separating hyperplane [39] as shown on Figure 3.4.

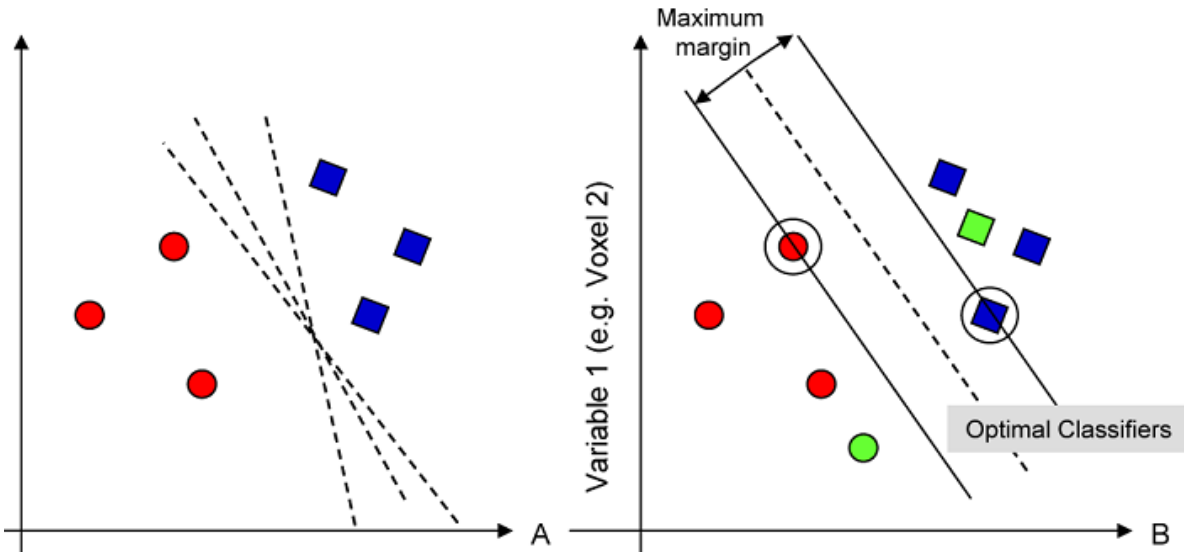


**Figure 3.4 - SVM training and classification. A) Hyperplanes found on the training phase. B) Optimal hyperplane found for classification. [37]**

It is also possible to assess the classifier performance by calculating its sensitivity and specificity, parameters that are usually analysed in order to conclude whether or not is better to use another classifier. According to the amount of well classified and misclassified subjects (true positive (TP) and true negative (TN), false positive (FP) and false negative (FN), respectively) the calculations are done as follows [40]:

Sensitivity = TP/(TP+FN)

Specificity = TN/(TN+FP)

# CHAPTER 4

## PARTIAL VOLUME CORRECTION

## *4.1. Partial Volume Effect*

The Partial Volume Effect (PVE) is an important degrading phenomenon in several PET and SPECT imaging applications such as oncology, cardiology and neurology. In the context of this thesis, PVE was studied and approached relative to AD PET imaging. Regarding this, the quantitative information of PET images is reduced and the degree of PVE is related to the size of the structure under analysis. The smaller the structure, the more severe PVE is [35], [41]. In quantitative studies, the tracer distributions are associated with the induced PVE distortions noticed in the images, both in the targeted and in the adjacent regions. The calculated time-activity curves (TACs) usually presents typical changes both in their magnitudes and shapes which results in errors of approximately 50% in estimated rate constants for transfer of tracer between compartments (assuming compartmental models, which were not part of this work) [42].

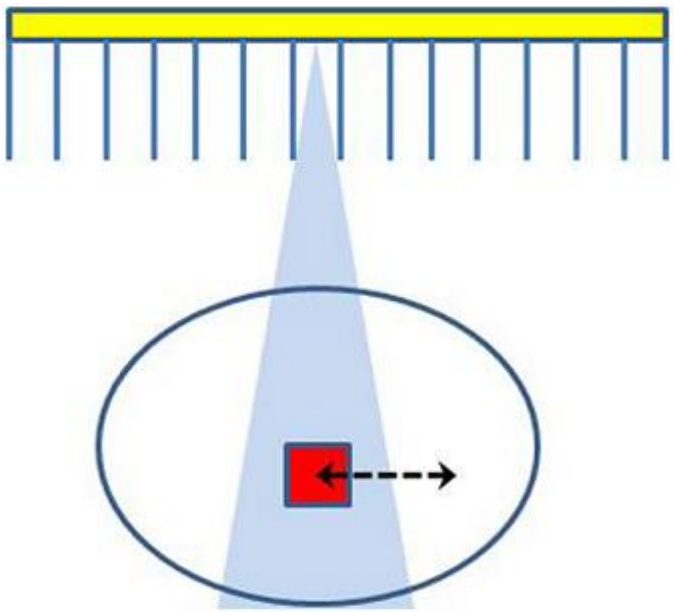

**Figure 4.1 - In PVE the small object of study (red square - real size) may partially occupy the sensitive volume (triangular shadow). The arrow represents the possible object motion during acquisition** [43]

In general, PVE does not cause a loss of information in terms of the total amount of counts in an image, i.e. the intensity of the image as calculated by radioactive activity. Instead, it displaces the values of activity between regions in the neighbourhood of the source region [35]. The most dangerous situation in neurology, particularly in AD, is that due to PVE some identified disease patterns might be lost, or diffuse enough to become hard to assess, leading to

erroneous diagnoses. As such, not only this effect has an impact on quantitative analyses, it also affects the use of SUV and SUVr images for diagnostic purposes.

There are two main reasons responsible for the occurrence of PVE in PET imaging, described below.

### 4.1.1. Scanner Point Spread Function

In general, PET scanners have a limited spatial resolution. The spatial resolution can be described as the ability to separate and detect two distinct objects, and this capability is related with the scanner Point Spread Function (PSF). In PET imaging, the image can be defined as a convolution of the true activity distribution with the scanner PSF. The PSF may be modelled by a 3-Dimensional Gaussian function that just depends on the Full Width at Half Maximum (FWHM) in the order of a few millimetres, which can be either the same or different in the different spatial directions [35], [44]. The spill-over effect (cross-contamination) between adjacent regions in images reflects the low spatial resolution and can be defined as the apparent gain of activity in some regions in contrast with others, and is divided in two distinct effects: spill-in and spill-out.

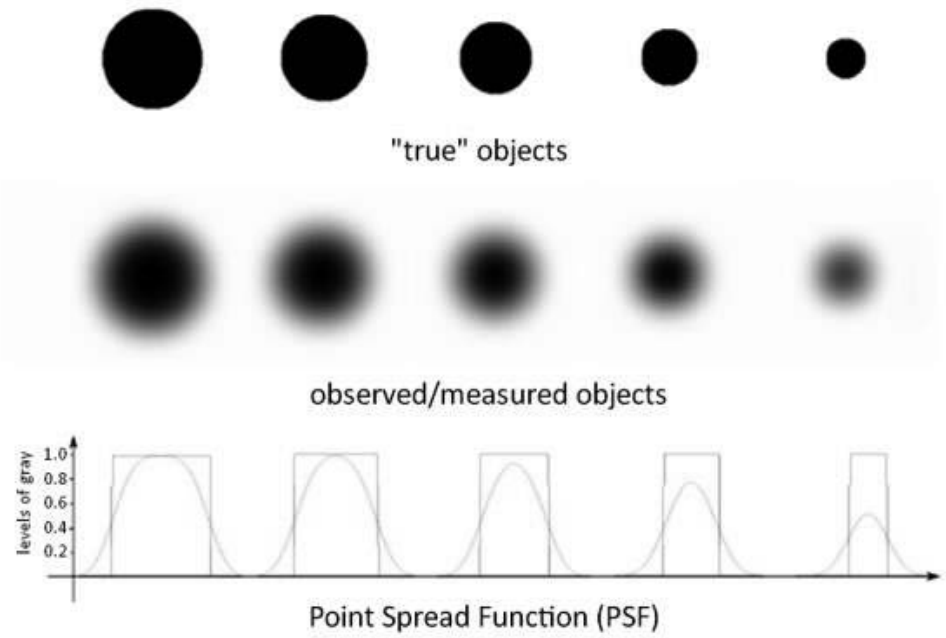


**Figure 4.2 - Point Spread Function Effect on true objects** [45]

This notation makes sense when examining small areas such as the ones analysed in the brain for AD diagnosis, and when it is essential to have precise information about the total activity in those areas, reflecting tracer concentration.

### 4.1.2. Tissue Fraction

PET images are displayed as a map of voxels, where each voxel dimensions are related to the PET scanner resolution and to the image reconstruction process, which is not discussed in this thesis. The placement of a geometrical sampling grid onto the variable geometry of the human anatomy, causes that within a voxel different types of brain matter may coexist [35]. In terms of image processing, this is due to the discrete sampling of images into finite voxels. This effect is known as the tissue fraction effect (TFE) [46]. The problem of this situation is that different brain tissues may have different tracer concentrations. Thus, each voxel may display the average activity of all the tissues contained on it instead of the true activity of a unique type of brain matter which is what is required with this measurements. Generally the mixture of brain tissues within a voxel includes grey matter (GM), white matter (WM) and cerebrospinal fluid (CSF). Usually, to correct this effects additional data is required so as to inform of the real underlying tissue locations, such as a high-resolution segmented MRI scan from the current patient. The coregistration of both images (PET and MRI) is necessary to perform the Partial Volume Correction (PVC) for this effect, using the algorithms described in the next paragraphs.

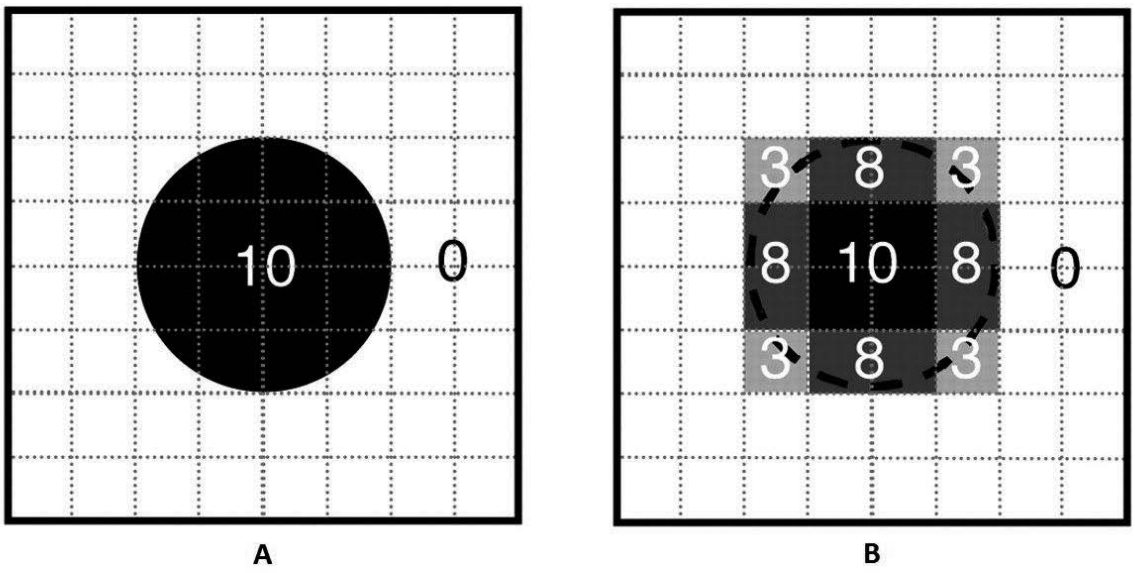


**Figure** 4.3 **- Tissue Fraction Effect on PET images** [47]

Figure 4.3 reflects the result caused by TFE on measured images. Image A is the real object with all the activity concentrated within the sphere. PET imaging systems do not know where the borders of the objects are, so during the image reconstruction pixels assume the activity concentration as the mean of the activity concentration within the pixel space. Thus, the result is a misdistribution of the true activity concentration on the final image, due to TFE. Some of the studied methods apply corrections to this effect.

## *4.2. Partial Volume Correction*

In the presence of PVE, neuroscientists and researchers felt the necessity of developing some techniques for correction such effects produced during the image formation. These techniques are called the Partial Volume Correction and were the main focus in the optimization of the analysis process described on this thesis. As explained before, there are two principal causes of PVE and these were the ones whose possible correction algorithms were addressed on this work.

The main goal of PVC methods is restoring the true activity distribution in PET images. Generically, a distortion of the real scenario is always intrinsic in imaging systems due to its electronics and image processing algorithms, usually transformed in the form of blurring and noise. PVC is useful in restoring as much as possible the original information that is trying to be sampled in images [48]. As will be explained in detail below, there are PVC methods to correct the effects due to either the PSF in separate or the PSF plus the tissue fraction effect.

## *4.3. Studied PVC Methods*

As told before, the main PVEs studied on this work were the tissue fraction effect and spill-over effect due to the PSF. Different PVC algorithms were implemented and the reason for this variety of studied methods were the analysis of the results achieved when correcting taking into account just the scanner PSF or both the scanner PSF and the tissue fraction. Depending on the used method, the obtained results can be different. Some methods provide corrected images, having as input the original uncorrected image and the scanner PSF (estimated or real – in all the implementation the PSF was estimated as 5.5mm FWHM isotropic 3D Gaussian function). Some other ones need as input segmented MRI data as well as the scanner PSF and the corrected

output are just values of the corrected ROIs. Next, all the implementations are described in detail with all the equations on which the algorithms are based on.

A statistical noise model is frequently associated to the image formation [49]. The noise in PET data derives from nature of radioactive decay and results on image deterioration. Some PVC methods take into account this typical noise while performing the corrections. Considering the observed image as $Y$, $X$ the ideal image reflecting the true activity distribution without PVEs and $H$ the scanner PSF, mathematically, the image $Y$ can be described as

$$Y(x) = \mathcal{N}_1(X \otimes H)(x) \qquad \textbf{Equation 4.1}$$

with $\otimes$ representing the 3 dimensional convolution operator and $x$ the 3D coordinate of an image voxel [50]. Generally some authors consider a second noise process $\mathcal{N}_2$ responsible for the noise amplification prior to the blurring by the PSF but that was not considered on the studied PVC techniques. Some of the following methods present iterative approaches of deconvolution-based algorithms (also referred as deblurring algorithms) that take into account different noise models (Gaussian and Poisson noise models). Their complete description will take place on the next sections.

### 4.3.1. Van Cittert

Van Cittert (VC) is the simplest PVC method implemented on this work [50]. It is based on a deconvolution process in order to restore the original information, removing the blurring effect and improving the contrast, imperfections created by the scanner PSF and visualized after the image processing. The disadvantage of deconvolution methods is the increased noise produced during the image correction, since they are iterative procedures and the noise levels increase proportionally with the number of iterations [51].

Based on the image reconstruction stated on Equation 4.1, the algorithm assumes as input the scanner PSF $H$ and the uncorrected image $Y$ on which the iterative deblurring algorithm will be applied. VC method suggests an approximate solution for $X$, since due to the statistical noise associated to the image formation, there is no exact solution. Thus, the algorithm proposed by VC, expressed in Equation 4.2, estimates $X$ as

$$X^{(i)}(x) = X^{(i-1)}(x) + \alpha\left(Y - H \otimes X^{(i-1)}\right)(x), X^{(i)} \geq 0 \text{ at each voxel} \qquad \textbf{Equation 4.2}$$

where $X^{(i)}$ denotes the estimation of the true image $X$ at the iteration $i$ and $X^{(0)}$ is the input image, $Y$. Figure **4.4** shows the typical differences possible to be observed on PET images when VC is used for PVC.

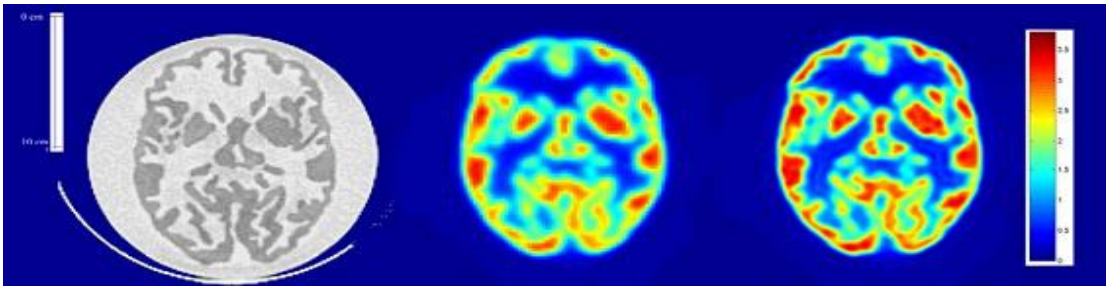

**Figure** 4.4 **- Van Citter PVC effect on PET images. Left: CT image; Middle: Original PET image; Right: PVC PET image. CT image can be used as reference image for comparison** [52]

There are some constraints that need to be fulfilled during this image correction procedure. First, as expressed in Equation 4.2, the voxels must be non-negative. Furthermore, there is a convergence factor $\alpha$, that usually ranges between 1 and 2 (herein set to 2), and the higher the convergence factor the faster the convergence is achieved. However, at some point the successive iterations lead to degradation in the corrected image due to excess of noise amplification produced by this inverse filtering solution, so a termination condition should be applied to stop the process when the maximum optimization is accomplished [41]. The condition, stated in Equation 4.3**,** is common to all the methods that apply a correction for the PSF effect and it follows the same structure, although the number of iterations and the stopping points are different because of the diverse levels of noise produced by the different algorithms during their performances.

$$\frac{\sqrt{\sum_x (X^{(i+1)}(x) - X^{(i)}(x))^2}}{\sqrt{\sum_x Y(x)^2}} \leq 0{,}01 \qquad \textbf{Equation 4.3}$$

This condition follows a voxel-wise convergence and when applying this criterion the algorithm may converge after 10-30 iterations [50]. However, if the convergence is not achieved until 100 iterations the algorithm is forced to stop. This subject will be discussed with more detail further on when the results are presented and examined.

### 4.3.2. Reblurred Van Cittert

This method is similar to the previous one. It follows a deconvolution iterative approach, although this is a technique based on a Gaussian noise model instead of a simple error-correcting procedure that does not rely on the optimization of any well-known statistical criterion [41]. It requires no anatomical information and it seeks a minimization of the least squares formulation stated on Equation 4.4.

$$\sum \|Y(x) - (X \otimes H)(x)\|^2 \qquad \textbf{Equation 4.4}$$

The direct solution for this criterion would be the inverse filtration but an iterative scheme for minimizing the gradient ensuring convergence is suggested in Equation 4.5 [35]

$$X^{(i+1)}(x) = X^{(i)}(x) + \alpha\,(H \otimes \left(Y - H \otimes X^{(i)}\right))(x) \qquad \textbf{Equation 4.5}$$

As like as in the method described in section 4.3.1, the algorithm proposed in the Reblurred Van Cittert (RVC) method has similar constraints to accomplish. The convergence criterion is the same voxel-based analysis and the convergence factor $\alpha$ was also set to 2 to achieve convergence faster. The algorithm needs the original uncorrected image and the estimated PSF as inputs and the voxels non-negativity is also necessary. $X^{(0)}$is the original image $Y$ like in VC method.

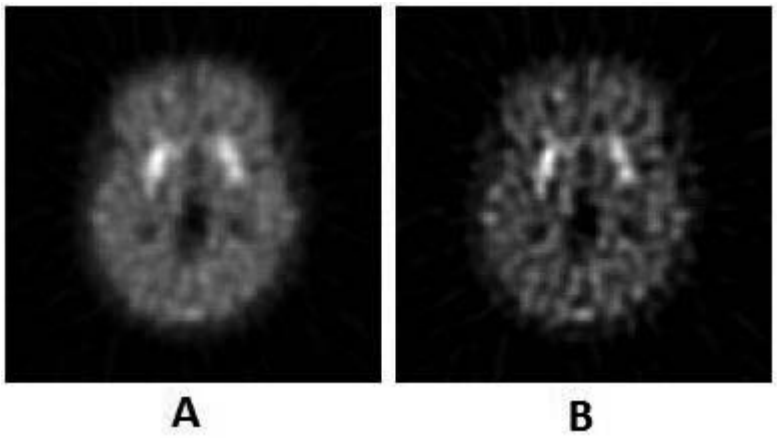


**Figure 4.5 - Effect of RVC PVC method on PET images. A) Original uncorrected image. B) RVC PVC corrected image. Adapted from** [49]

The main advantage of deconvolution-based techniques such as VC and RVC is the speed of processing and the ease to implement on image processing algorithm. Nevertheless they amplify the noise to enormous proportions [35], [41], [50]. At some level of convergence the process needs to be stopped to ensure the solution quality. After analysing the results efforts

were made to reach some ways of controlling the moment for stopping the iterative progressions in addition to the convergence criterion. These ways will be explained later on results discussion.

### 4.3.3. Richardson-Lucy

This PVC method presents another class of deconvolution iterative approaches. Richardson-Lucy (RL) is based on the Poisson noise model and on the maximum likelihood principle [41]. The noise is intrinsic to the counting statistics and each voxel is drawn independently from the noise distribution.

The log-likelihood this algorithm intends to maximize is given by Equation 4.6

$$l(X) \propto \sum_x [Y(x) \log(X \otimes H)(x) - (X \otimes H)(x)] \qquad \textbf{Equation 4.6}$$

This method uses the Expectation Maximization (EM) algorithm to maximize the log-likelihood given by the previous equation and it is accomplished with the following iterative rule

$$X^{(i+1)}(x) = (S \otimes H)(x) X^{(i)}(x) \qquad \textbf{Equation 4.7}$$

where $S$ is given by

$$S(x) = \frac{Y(x)}{(X^{(i)} \otimes H)(x)} \qquad \textbf{Equation 4.8}$$

As like as in the previous models, in the first iteration $X^{(0)}$ is estimated as being the observed image $Y$.

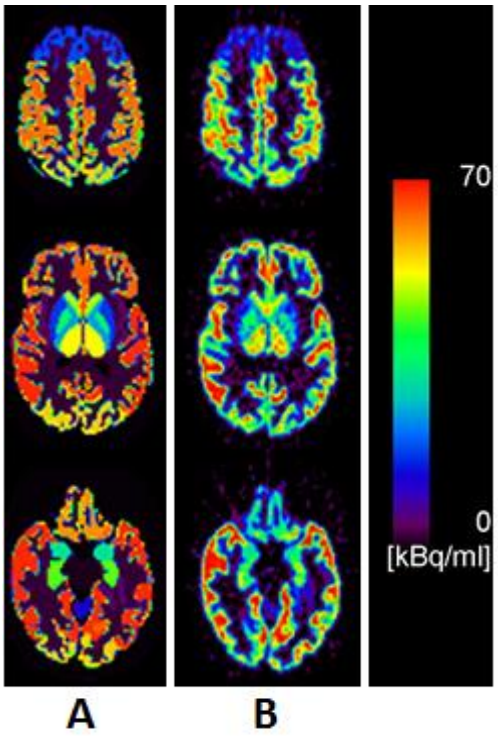


**Figure 4.6 - Richardson Lucy PVC method. A) Original image; B) RL corrected image. Adapted from** [53]

The initial non-negativity is also required and the algorithm itself preserves the positivity and the total amount of counts, i.e. $X^{(i)}(x) \geq 0$ if $X^{(i-1)}(x) \geq 0$ and $\sum_x X^{(i)}(x) = \sum_x X^{(i-1)}(x)$ [49]. In order to avoid the noise amplification common on deconvolution algorithms, the convergence criterion stated on Equation 4.3 is also applied here. The main advantages are the ease to implement, the no necessity of anatomical data and the speed of processing until the convergence to the maximum likelihood solution is achieved [54]. The results obtained from this method implementation will be shown and discussed later on.

### 4.3.4. Müller-Gartner

Müller-Gartner (MG) PVC method is based on different assumptions comparing with the former ones (VC, RVC and RL). This one described a PVC approach directed to GM correction specifically. Due to the physics of PET systems, brain structures such as GM, WM and CSF are often mixed in the same voxel and consequently the tracer concentrations are often underestimated [55], including the GM brain structures known as the most affected ones in AD.

This MR-based PVC method requires a MRI scan to assess the regional anatomical structures. The MRI scan has to be properly segmented in order to provide the tissue maps that

are not available on PET image [56]. The image formation basis is the same as the one stated in the previous sections (Equation 4.1) and the algorithm mathematical formulations assume the total radioactive distribution displayed by the true image as the linear sum of radioactive distribution of the three brain matters GM, WM and CSF as follows

$$X_{total}(x) = (X_{GM} + X_{WM} + X_{CSF})(x) \qquad \textbf{Equation 4.9}$$

From Equation 4.1 and Equation 4.9 and due to the nature of the convolution the observed image can be written by

$$Y(x) = X_{GM} \otimes H + X_{WM} \otimes H + X_{CSF} \otimes H\ (x) \qquad \textbf{Equation 4.10}$$

As said before, this method results on the correction of only the GM. Because of this, it is assumed that GM tracer concentration is unknown, in contrast to WM and CSF radiotracer concentrations which are assumed to be constant and known. $MR_{tissue}$ is the segmented MRI scan. It is a binary image that contains 1 on voxels representing the tissue and 0 otherwise. Thus

$$\begin{aligned} X_{WM}(x) &= \bar{X}_{WM} MR_{WM}(x) \\ X_{CSF}(x) &= \bar{X}_{CSF} MR_{CSF}(x) \\ X_{GM}(x) &= \bar{X}_{GM} MR_{GM}(x) \end{aligned} \qquad \textbf{Equation 4.11}$$

where $\bar{X}_{tissue}$ represents the tracer concentration within the tissue. $\bar{X}_{GM}$ is also unknown so it cannot be used in the algorithm formulations. Using the above equations and substituting them on Equation 4.10, the observed image is given by

$$Y(x) = X_{GM} \otimes H + \bar{X}_{WM} MR_{WM} \otimes H + \bar{X}_{CSF} MR_{CSF} \otimes H\ (x) \qquad \textbf{Equation 4.12}$$

and solving Equation 4.12 in order to achieve a solution to $X_{GM}$ it becomes

$$X_{GM} \otimes H(x) = Y - \bar{X}_{WM} MR_{WM} \otimes H - \bar{X}_{CSF} MR_{CSF} \otimes H\ (x) \qquad \textbf{Equation 4.13}$$

Using Equation 4.11 and the properties of the 3D convolution operator,

$$(\bar{X}_{tissue} MR_{tissue}) \otimes H\ (x) = \bar{X}_{tissue} (MR_{tissue} \otimes H)(x) \qquad \textbf{Equation 4.14}$$

it is possible to yield a solution for $\bar{X}_{GM}$ as stated on Equation 4.15

$$\bar{X}_{GM}(x) = \frac{Y - \bar{X}_{WM} MR_{WM} \otimes H - \bar{X}_{CSF} MR_{CSF} \otimes H\ (x)}{MR_{GM} \otimes H(x)} \qquad \textbf{Equation 4.15}$$

Since $\bar{X}_{WM}$ and $\bar{X}_{CSF}$ are assumed to be constant and homogeneous within the correspondent tissues, some modifications need to be done. Their voxels are replaced by the average of the PET

counts, respectively. If these changes are not made it is not valid to estimate $\bar{X}_{GM}$ by Equation 4.15 due to the heterogeneity of $\bar{X}_{WM}$ and $\bar{X}_{CSF}$ [55].

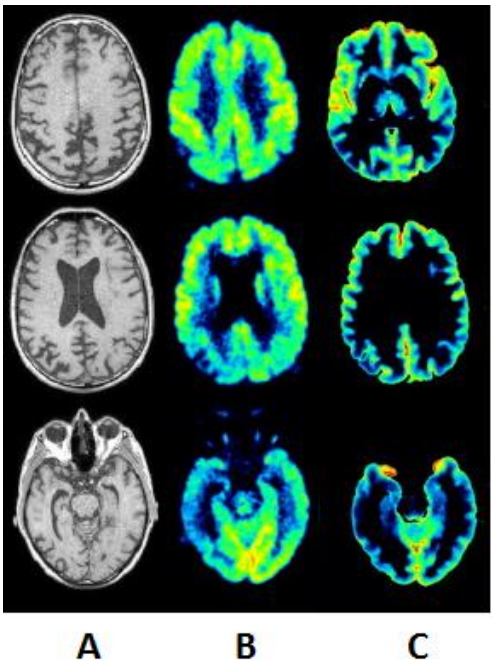


**Figure 4.7 - Partial Volume Correction by MG method with grey matter segmentation. A) Original MRI scan used for segmentation; B) Original PET brain image; C) MG PVC corrected image (grey matter). Adapted from** [57]

This method presents a voxel-wise correction only for GM structure that takes into account the tissue fraction effect in addition to the PSF effect. Apart from the previous methods, this one requires a trisegmented MRI scan and a proper PET-MRI image registration, and it is not an iterative approach. However, the accuracy of this MR-based PVC method may be affected by several sources of error [56]. The misregistration of the MR and PET volumes and the inaccurate segmentation of the MR scan into the necessary brain tissue compartments, with consequent over/underestimation of structure volumes and finally under/overestimation of GM tracer concentration, respectively, are actually the most common causes of unfeasible results.

### 4.3.5. Rousset

Appart from all the PVC methods described so far, Rousset does not provide corrected images, but corrected values for the tracer concentrations on specific ROIs, previously selected

with the MRI data support. Similar to MG, Rousset on its approach considers the PVEs caused by the tissue fraction and the scanner PSF [58]. The origins of both effects have already been explained so, on this section just the formulations and approaches suggested by this method will be presented.

The image formation expressed by Equation 4.1 is here assumed in the form of a weighted integration of the activity distribution $f(r)$ over the scanner FOV, by the PET system response function in the form of PSF, $H$, as follows:

$$g(r) = \int_{FOV} f(r')H(r,r')dr' \qquad \textbf{Equation 4.16}$$

having $r$ and $r'$ as the 3D vectors on image and object reference spaces, respectively [42]. The true activity distribution $T_i$, which is what one seeks to find, is likely to be distributed over several tissue components, defined by the domain $D_i$, and the Equation 4.16 can be written as

$$g(r) = \sum_{i=1}^{N} \int_{D_i} T_i(r')H(r,r')dr' \qquad \textbf{Equation 4.17}$$

where N is the amount of tissues over which $T_i$ is distributed. On each tissue domain $D_i$ the activity distribution $T_i(r)$ is assumed to be constant, thus the integration remains only over the scanner PSF

$$g(r) = \sum_{i=1}^{N} T_i \int_{D_i} H(r,r')dr' \qquad \textbf{Equation 4.18}$$

and the integration of the PSF over a regional domain $D_i$ is the same of having a regional spread function (RSF) correspondent to that domain

$$RSF_i(r) = \int_{D_i} H(r,r')dr' \qquad \textbf{Equation 4.19}$$

A great advantage of using this method is the possibility of assessing the domain of calculation to the specific ROIs to be corrected. If the correction was directed to the total tissue compartment, for instance GM, the spillover effect of small structures within GM would not be accounted for, and the small activity contaminations between adjacent structures would remain uncorrected. This way, Rousset restricts the spatial domains to ROIs instead of the total tissue compartments such as MG does [42]. In order to perform this ROIs segmentation accurately, the segmented MRI scan is essential.

Assuming the observed activity concentration $t_j$ within each $ROI_j$ as the sum of the activity contributions from the regional domains, it can be expressed as

$$t_j = \frac{1}{n_{vox}} \sum_{i=1}^{N} T_i \int_{ROI_j} RSF_i(r)dr \qquad \textbf{Equation 4.20}$$

where $n_{vox}$ is the amount of voxels on $ROI_j$ and $i$ represents the index of the regional domain whose activity contributes to the observed activity $t_j$. Equation 4.20 can be described as the multiplication of the true activity concentration by a weighting factor that depends on the region domain that provides the contribution. Since $\frac{1}{n_{vox}}$ is constant for each $ROI_j$ the contribution factor is expressed by

$$w_{ij} = \frac{1}{n_{vox}} \int_{ROI_j} RSF_i(r)dr \qquad \textbf{Equation 4.21}$$

and represents the relative contribution of each domain $D_i$ to each $ROI_j$ of the image. In other words, it represents the activity concentration that is spilled over the domain $D_i$ and is assumed as part of the observed activity concentration of $ROI_j$. Thus, the observed activity concentration can be written by the following expression:

$$t_j = \sum_{i=1}^{N} w_{ij} T_i \qquad \textbf{Equation 4.22}$$

Moreover, Equation 4.22 can be extended into the matrix like $t = wT$

$$\begin{bmatrix} t_1 \\ t_2 \\ \vdots \\ t_x \end{bmatrix} = \begin{bmatrix} w_{1,1} & w_{2,1} & \cdots & w_{x,1} \\ w_{1,2} & w_{2,2} & \cdots & w_{x,2} \\ \vdots & \vdots & \ddots & \vdots \\ w_{1,x} & w_{2,x} & \cdots & w_{x,x} \end{bmatrix} \begin{bmatrix} T_1 \\ T_2 \\ \vdots \\ T_x \end{bmatrix} \qquad \textbf{Equation 4.23}$$

Analyzing Equation 4.23 in detail it is possible to create a system of linear equations with $t$ and $w$, solving it in order to identify the values of $T$ that represent the true activity concentration in each specific ROI. $w$ is known as the Geometric Transfer Matrix (GTM) and it is easy to understand that diagonal factors represent the ROIs self-interaction so they are expected to be the highest values of the respective line of GTM.

A great advantage of applying this method is that it does not perform the deconvolution procedure used on the VC, RVC and RL methods, which result in noise amplification. Previously studied and reviewed [42], [58], Rousset method yields results that assure the accuracy and capability of providing corrected activity concentrations even for small structures/ROIs

surrounded by background activity. Similar to MG, misregistration and missegmentation are common sources of error. Misregistration has already been studied and reported an error of approximately 5% of true activity per mm of axial misregistration [42].

The analyzed ROIs and respective values achieved with Rousset method will be discussed and compared with the other PVC methods ahead.

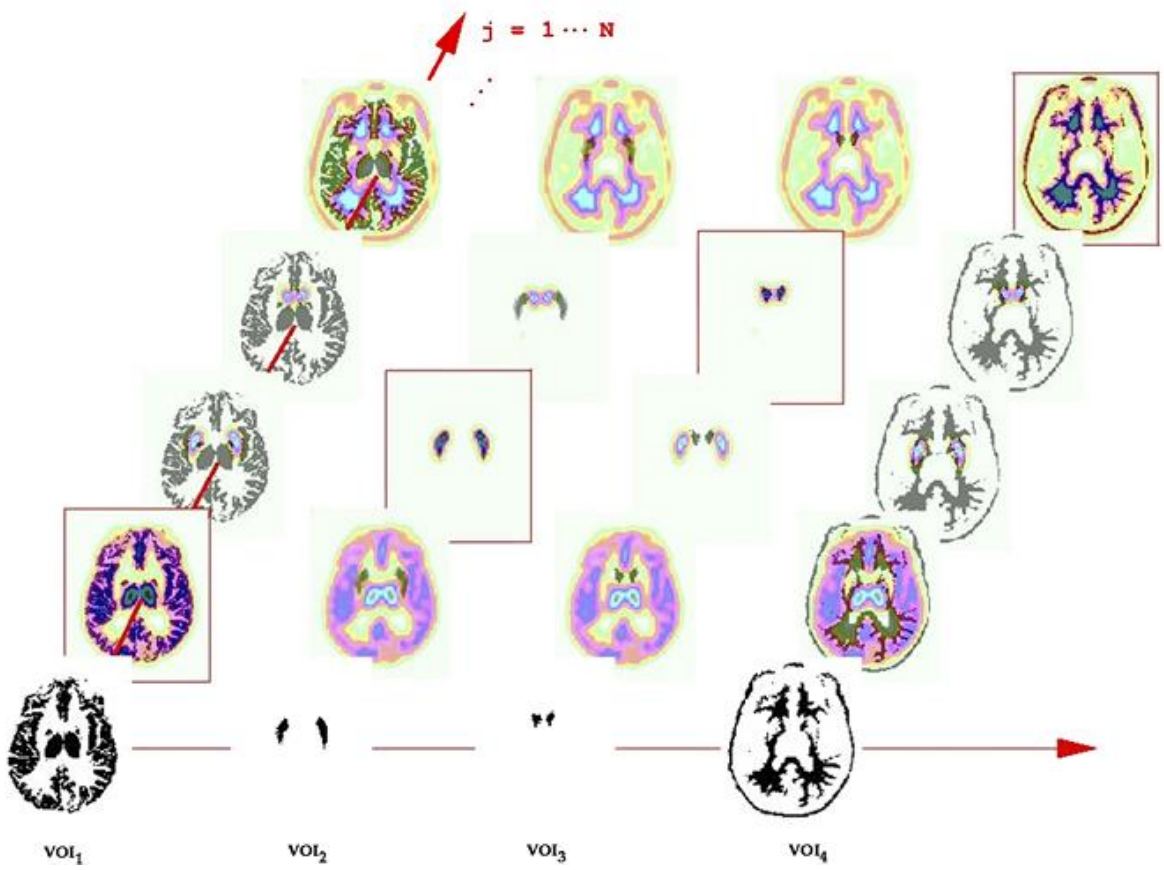


**Figure 4.8 - GTM estimation. The lines represent the intersection of each RSF with the ROIs (expressed by VOI) of each collumn.** [58]

# CHAPTER 5

## PIPELINE OPTIMIZATION

## *5.1. MRI and PET image acquisition protocol*

MRI and PET data are obtained on Nuclear Sciences Institute Applied to Health, University of Coimbra (ICNAS) facilities using different systems with the respective acquisition protocols. MRI scans are performed on a Siemens Trio 3T system (Siemens Medical Systems, Erlangen, Germany) achieving T1-weighted anatomical acquisitions 92x192x144 slices with a voxel resolution of 1.25x1.25x1.25mm3, and consisting of 3D magnetization prepared, rapid gradient-echo (MPRAGE) volumes with the following imaging parameters: repetition time/echo time/inversion time/flip angle = 2300ms/2.86ms/900ms/9º, lasting less than 8 minutes.

PET acquisitions for PiB were also optimised at ICNAS. PET scans are acquired using the Philips Gemini GXL 16 PET/CT scanner. For PiB acquisitions, patients are injected with 15mCi of 11C-PiB. Dynamic acquisition starts immediately after injection and lasts for 90 minutes, with data acquired in multiple frames with increasing duration (4x15s, 8x30s, 9x60s, 2x180s, 14x300s). Data are reconstructed using the standard clinical protocol (3D LOR-RAMLA) with all standard corrections applied. Final attenuated corrected images are in Standard Uptake Values (SUV).

In this context, the frames are 3D volumes that contain the acquired data during the respective acquisition time interval. The acquisition protocol defines how many frames are generated as the output. PET acquisition protocol may vary depending on what is required on the study. The static protocol consists of only 30 minutes of acquisition, with 6 frames of 5 minutes each one. In this case, after the tracer injection, the patient rests for 40 minutes and in the next 30 minutes the acquisition is performed. This 40-70mins time window is used due to the signal stability achieved here, as explained before. However, although the obtained signal is very amyloid specific on this interval, this protocol does not allow for quantitative studies. Therefore the dynamic protocol is necessary for research purposes and can also be used for basic clinical purposes, as it includes the static protocol within.

Quantitative methods use the Time Activity Curve (TAC) to indirectly estimate the input function of PiB studies [27]. In this case, the reference region is the cerebellum and the TAC is measured over time as an expression of the average cerebellum PiB retention (Figure 5.1) As such, both for the quantitative analyses (not expanded in this thesis) and for the calculation of SUVr, a properly registered cerebellar mask is necessary. The registration procedures will be addresses in the next section.

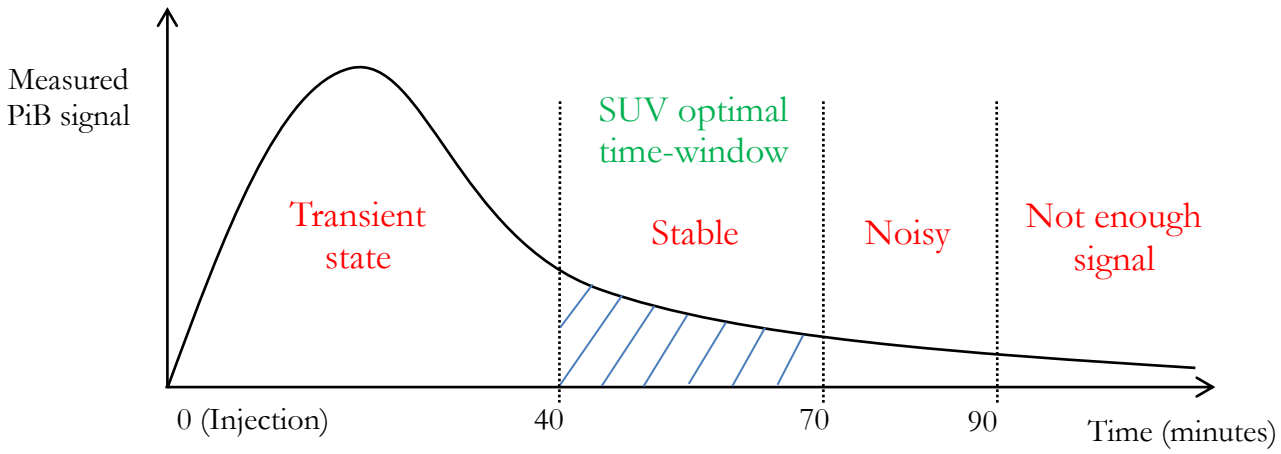


**Figure 5.1 - Typical Time Activity Curve expressing the radiotracer uptake in function of time**

## *5.2. Image Registration and Image Spaces*

Registration procedures are necessary when taking into account differences between image spaces: they involve the optimal estimation of spatial transformations, and subsequent application of these on the images, required to transfer an image to the space of a target. Here, two modalities are being used (MRI and PET) and the images provided by them present a different arrangement of the head of the patient, since its position during the acquisitions is also different. In other words, the *native spaces* on MR and PET images are different as shown on Figure 5.2: one must be chosen as the working space, thus requiring the registration of one image to the other.

Registration between MR and PET involves rigid-body transformations. A rigid transformation is a type of linear registration. A linear registration works globally on an image, i.e. all coordinates **x** are transformed in the same way by the multiplication with a matrix **T**, which includes the transformation parameters, leading to a new volume with new coordinates as expressed by Equation 5.1

$$\mathbf{x_f} = \mathbf{T}\mathbf{x_i} \Leftrightarrow \begin{bmatrix} x_f \\ y_f \\ z_f \\ 0 \end{bmatrix} = \begin{bmatrix} & \mathbf{P} & & \mathbf{t} \\ 0 & 0 & 0 & 1 \end{bmatrix} \begin{bmatrix} x_i \\ y_i \\ z_i \\ 0 \end{bmatrix} \qquad \textbf{Equation 5.1}$$

where **P** represents a 3x3 matrix describing the rotations, shears and scaling, and **t** is a 3x1 vector that contains the parameters relative to the translations. This full transformation, with all 12 parameters involved in three dimensions, is also called an affine transformation. The last row of

**T** is added just to assure that the matrix is square and therefore easily invertible in a single computational step, adding to efficiency [59]**.**

The rigid-body transformation is a particular case in which **T** only contains rotations and translations, preserving the angles and distances of the image to be registered [60].

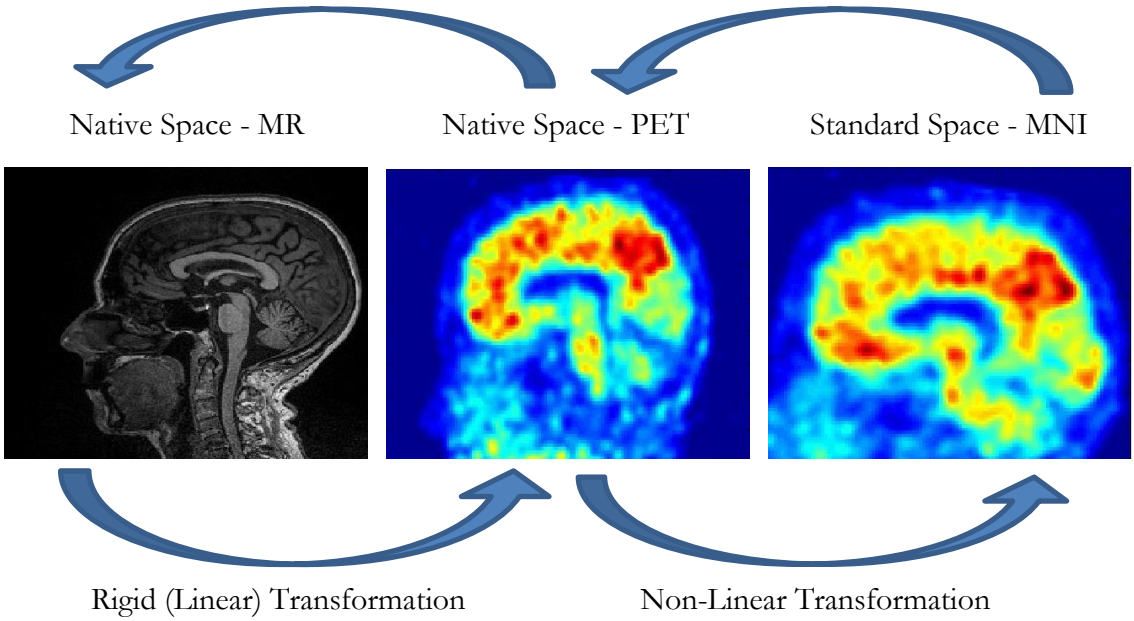


**Figure 5.2 - Spatial transformations of images**

In a rigid transformation, three rotations (about the x, y and z axes) and three translations (in x, y and z directions) are allowed, without any scaling factor. Thus, the rigid-body registration only accounts for gross differences in position, the actual repositioning of a non-deformable body.

Finally, the use of non-linear registration occurs when coordinates need to be changed individually, i.e. $\mathbf{x}_f = \mathbf{T}(\mathbf{x}_i).\mathbf{x}_i$ to use the nomenclature above. This is required when the target space is not only globally, but also locally different, from the image to be registered, as it happens when registering brain scans from different individuals or when using standard spaces, for instance. It is applied when is essential to ensure that similar brain structures are represented in the same location on the standard space. Therefore, the degrees of freedom given by the linear registrations are not enough and herein, many degrees of freedom are used to perform a finer registration. On non-linear registrations each voxel undergoes a displacement that may not be the same of the surrounding voxels [61]. However, care is needed when performing this type of

image registration on anatomical images. The amount of degrees of freedom may be such that the deformation produced on images can generate an output with no anatomical meaning.

The existence of a standard space is useful when comparisons among a group of scans are necessary for statistical purposes, or simply to report data on an internationally recognized atlas or template. Additionally, these atlas also include regions of interest (ROIs) that can be used to extract data from specific brain locations: as these ROIs are in a standard space, either the standard space is registered to the subject native space or, more common, it is the individual scan that is, non-linearly, registered to the template. In this case, the used standard space is the one provided by Montreal Neurologic Institute (MNI) atlases, notably the ICBM152 (International Consortium for Brain Mapping template based on the average of 152 brains).

## *5.3. Pipeline Overview*

The initial work of this thesis involved the improvement of the previously developed pipeline of analysis for SUV and SUVr data. This was achieved by using the software MATLAB (The Mathworks Inc., Natick, MA, USA) and related software, notably the Statistical Parametric Mapping 8 (SPM8, www.fil.ion.ucl.ac.uk/spm/). SPM is a widely used software for processing and analyzing brain imaging data. Different imaging modalities may be analyzed using SPM, although all the usage of this package relied on MRI and PET data in this thesis. This chapter focuses on the enhancements performed on the original pipeline whose interface is shown in Figure 5.3. Some other options were introduced into the pipeline and a modified interface was developed. The PVC methods integration on the pipeline was the most important task, in addition to the improvements in the image registration process, as explained ahead. The differences between the original and the modified interface, as well as the pipeline options, will be explained in detail in this section.

As shown on the pipeline fluxogram, presented on Figure 5.4, the analysis can be divided into three different parts. On the first part an initial processing is performed, where the raw data files containing the acquisition information are converted from DICOM format, the standard raw data format for images in the scanner, to NIFTI (*.nii) or the older dual file ANALYZE (*.img and *.hdr) format, both necessary for seamless usage in SPM and MATLAB. This procedure gives as output the frame sequence that corresponds to the information contained on the DICOM files - numerous and fragmented - and the output files (4D or 3D volumes) can be opened in the form of images showing the results of acquisition. The frame sequence is then

realigned to correct for the motion that is usually present on PET acquisitions. After this, all PET frames (each a 3D image volume) are rigidly aligned to each other and to their mean so as to remove any motion artifacts brought about by the subject moving during the long acquisition time. With this, the first part of the analysis is done.

The second part consists on the spatial conversions when the user can choose either to create a PET native space reference or use the MR as the working native space reference (if available), for the image registration procedures. On the first case, the first 10 minutes of acquisition are used to create the reference since this is the period where the PiB signal is higher, as shown on Figure 5.1, due to the initial perfusion of the radiotracer in the head. On the other hand, it is possible to use the MR scan as the native space reference, which is ideal given its higher resolution and greater potential for non-linear deformation when (if) registering to MNI afterwards. In these cases, the PET data is registered to the MR scan through the linear registration procedures as explained above on section 5.2.

Finally, if MNI is chosen as output, the working native space reference, be it PET or MR, will be used as basis for the required non-linear transformation using the ICBM152 template as target. It should be noted that such a non-linear transformation is required regardless of the choice of output space. Indeed, if the images are to remain and be analyzed in their original space, the cerebellar and other eventual ROI masks, which exist in MNI space, must still be registered from MNI to native PET or MR space in order to be used in the final steps of the analysis: this is achieved in SPM8 by estimating the non-linear deformation parameters that define the native to MNI registration, inverting them (i.e. MNI to native), and then applying them to the individual binary masks.

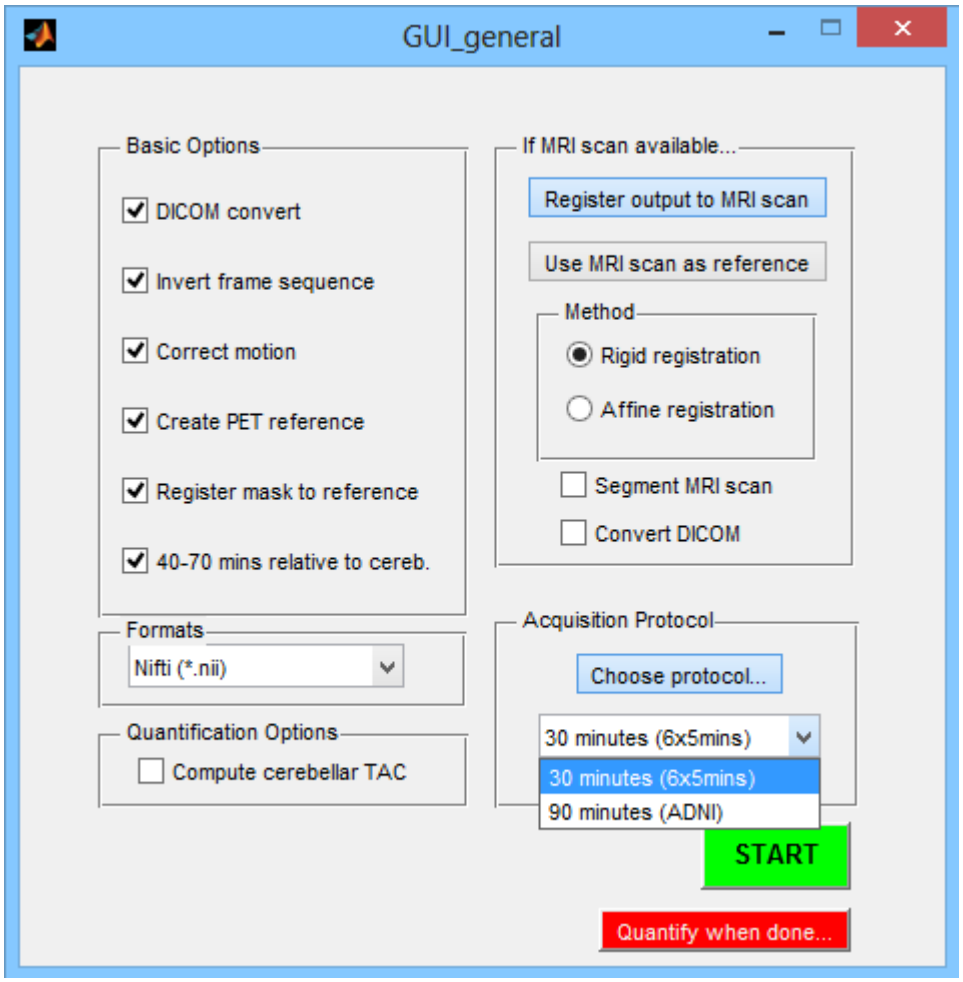


**Figure 5.3 - Interface of original pipeline**

The last part of the analysis is the calculation of the outputs. Here, the masks are applied in order to calculate SUVr from 40 to 70 minutes, extract the ROI values, or compute TACs.

However, the original pipeline was identified to have some limitations. These limitations can be found on the frame realignment, image registration procedures, as well as on the final calculations. These were improved, as described below.

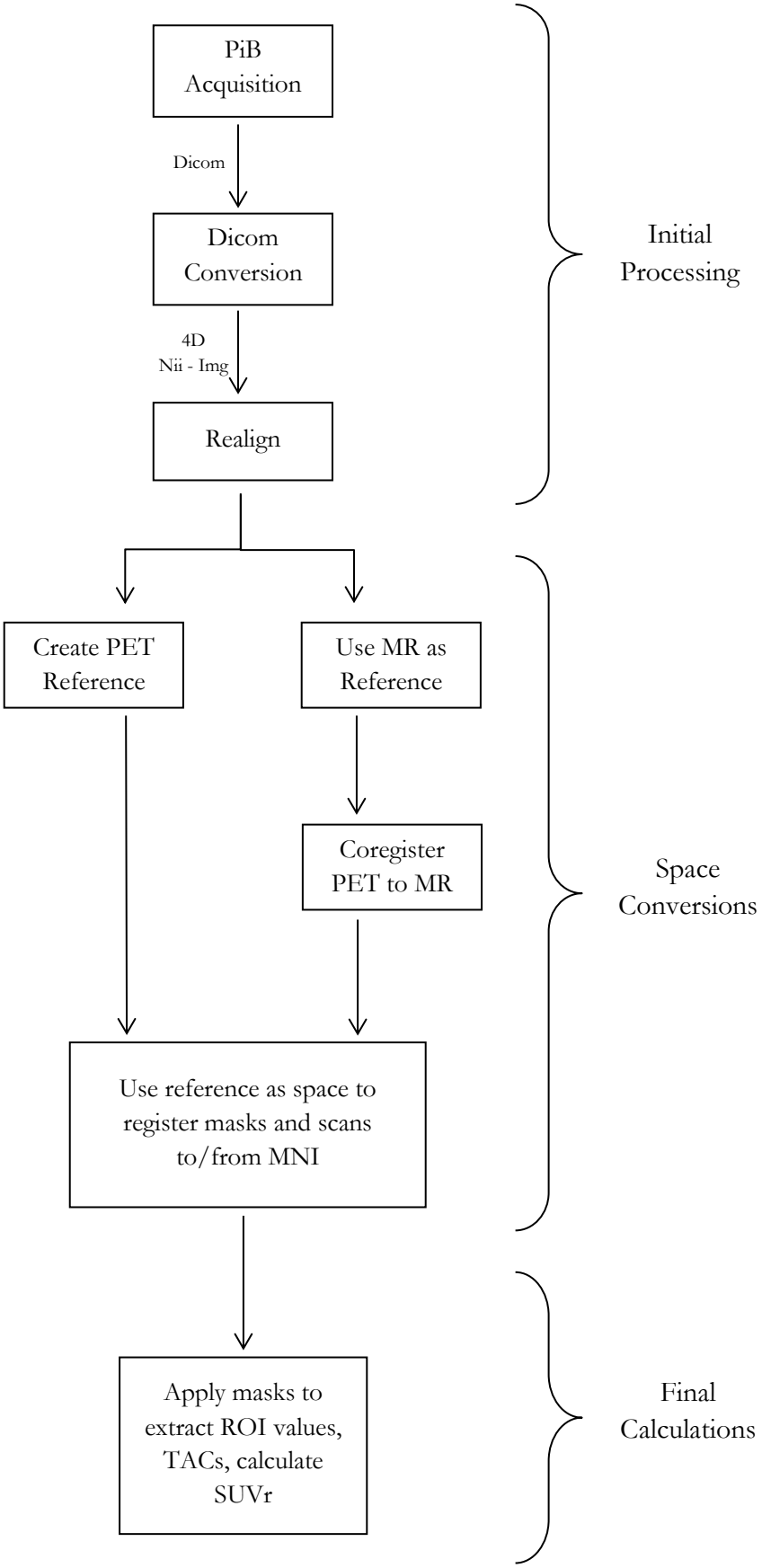


**Figure 5.4 - Simplified Pipeline Fluxogram**

## *5.4. Pipeline Improvements*

### 5.4.1. Frame Realignment

In the original pipeline, the frame realignment was being performed through the standard SPM8 method, which is open to issues when using dynamic PET data. In this method, one by one, all the frames are registered to the first frame, then the result is summed and the reference for the second alignment pass is the average of all the frames. All the images are rigidly registered to this reference to achieve a consistent alignment of the frames. This two pass procedure may fail if the first pass finds an empty first PET frame, or at least one with few counts and thus little spatial detail to guide the process. This is an issue in dynamic protocols because, in the first frames, the radiotacer perfusion is still at the beginning.

An initial improvement was to look for positive values of retention within a central block of voxels in the first frame. If this block was not empty, then one could postulate that the frame had enough information in it and was not empty, so it could be used in the standard method. If no positive values were found, this frame would be ignored and the second frame would be considered the first, using only the following frames for the realignment.

Because sometimes the first few frames were empty rather than just the first, this function was further optimized using the Jaccard Coefficient to statistically compare the five initial frames to the central one (in this case, the dynamic acquisition is divided into 37 frames, consequently the central frame is the frame 19). This coefficient is calculated with the formula stated on Equation 5.2

$$Jaccard\ Coefficient\ (A,B) = \frac{|A \cap B|}{|A \cup B|} \qquad \textbf{Equation 5.2}$$

where A and B are the subsets whose overlap is necessary to be estimated [62], [63].

The calculation is performed using binarised volumes, where the threshold for the binarization is the average of the voxels values. This coefficient measures the overlap between the initial frames and a middle frame, that is certainly not empty: if this overlap is above a certain level (heuristically set at 0.2 in this case), the frame is not empty and can be used for realignment; if below, then it can be considered empty, or at least without enough spatial information, and is discarded. These discarded frames are still used in the subsequent processing, they are only eliminated for the realignment step. This analysis is now extended to the first five frames, covering approximately the first minute of acquisition (5x15s – assuming dynamic protocol), as

opposed to the original function that was only analyzing the first frame (first 15s). Figure 5.5 shows the different alignment of the same slices of a frame when using the original and the current methodology. This is an example of what may happen when the verification is just done to the first frame. The following ones may do not have enough information for a proper realignment and the differences are obvious. This is an important improvement that has effect on the following steps of the analysis.

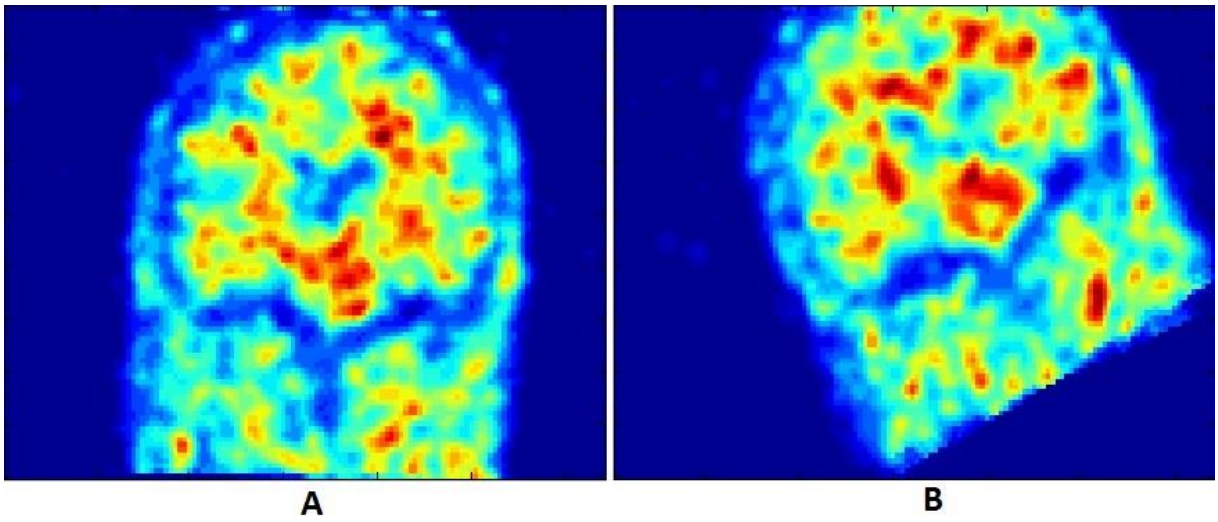


**Figure 5.5 - Results of frame realignment methodologies. A) Slice of a frame realigned with the current function. B) Same slice and frame realigned with the original function.**

### 5.4.2. Image Registration

Another point that is improved is the image registration. Originally, it was impossible to have the output volumes registered to the standard space. This option was added and now the user can choose to register the final output to the MNI space, having already available the templates for the image registration. In addition, the user can choose the ROIs (from a list previously provided) which are going to be used in the final calculations steps, and these masks are registered together with the cerebellum to the native space, as described above (or remain in MNI, if that is the choice). All the ROIs are originally on the MNI space.

### 5.4.3. Final Calculations

An important part of the pipeline improvement was done on the final steps with the implementation of the partial volume correction. Five different methods were implemented and

the user can choose which ones are going to be performed. The type of the final output can also be chosen: ROI values, SUVr images or both, with the exception of Rousset method that only provides ROI values. If Rousset or MG are between the choices of PVC methods to be performed, the program chooses automatically to use the MR as reference space, since these methods need the MR scan as explained in section 4.3. Figure 5.6, Figure 5.7 and Figure 5.8 show the windows of the current interface.

Another goal was the pipeline extension to analyze different radiotracers beyond PiB. This extension was achieved as shown on Figure 5.7 where it is possible to choose between Flumazenil, Raclopride and FDG in addition to PiB. For these radiotracers the protocols of acquisition might not be the same as the ones used with PiB so the user can also select to input the acquisition protocol in order to perform the convenient analysis. The reference region also varies depending on the used radiotracer. In the case of PiB, Raclopride and FDG, cerebellum is used as the reference region by the reasons explained above on chapter 3, however, when using Flumazenil, pons is used as the reference region rather than cerebellum [29], [64], [65], [66].

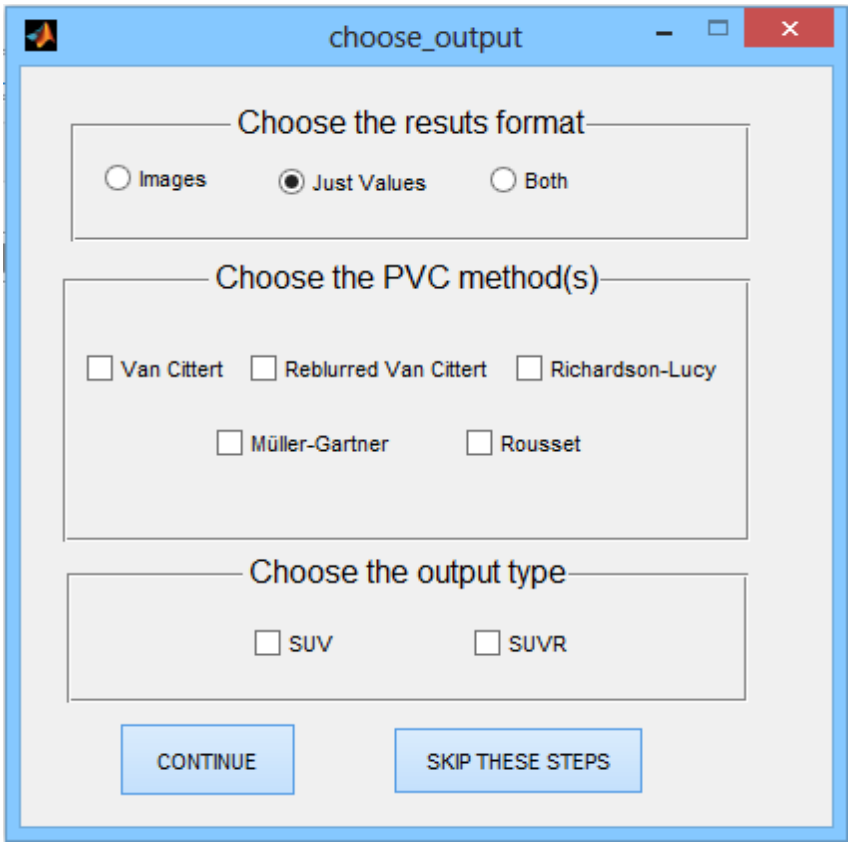


**Figure 5.6 - Interface to choose the type of PVC output (images, ROIs values or both), the PVC methods to be performed, and the volumes to apply PVC (SUV or SUVr)**

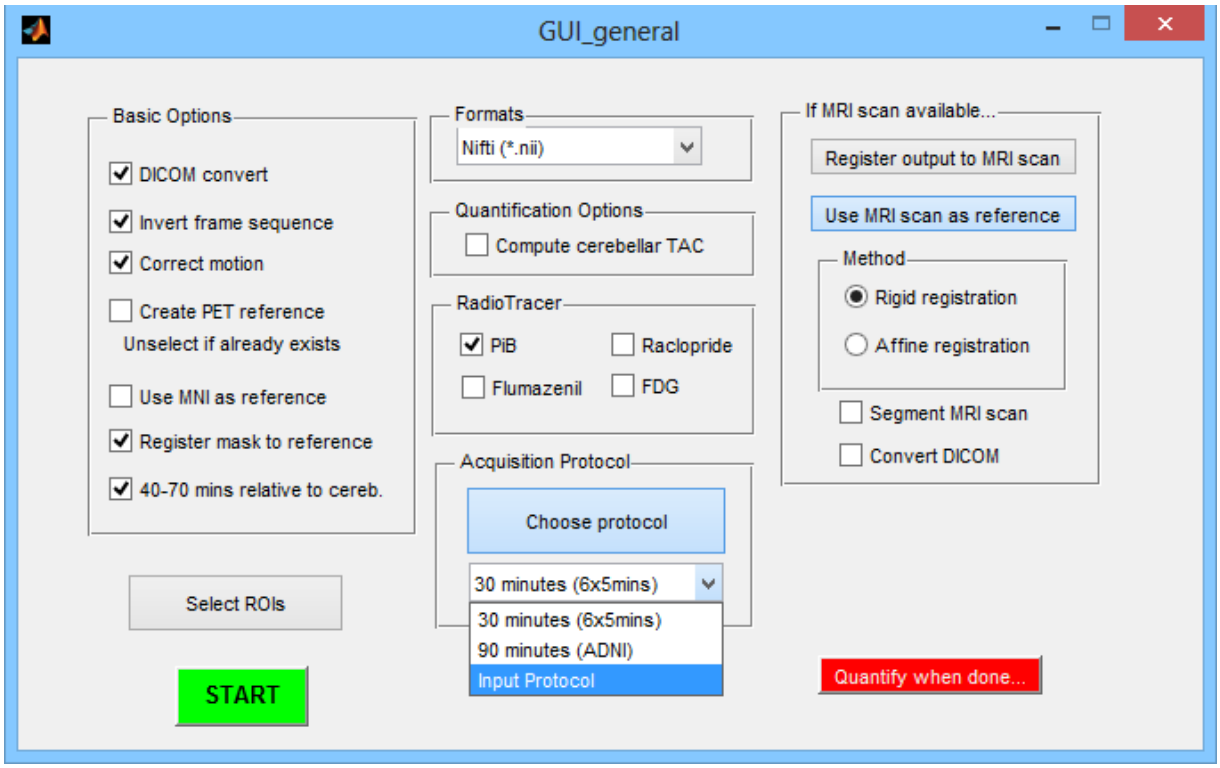


**Figure 5.7 - Actual main interface**

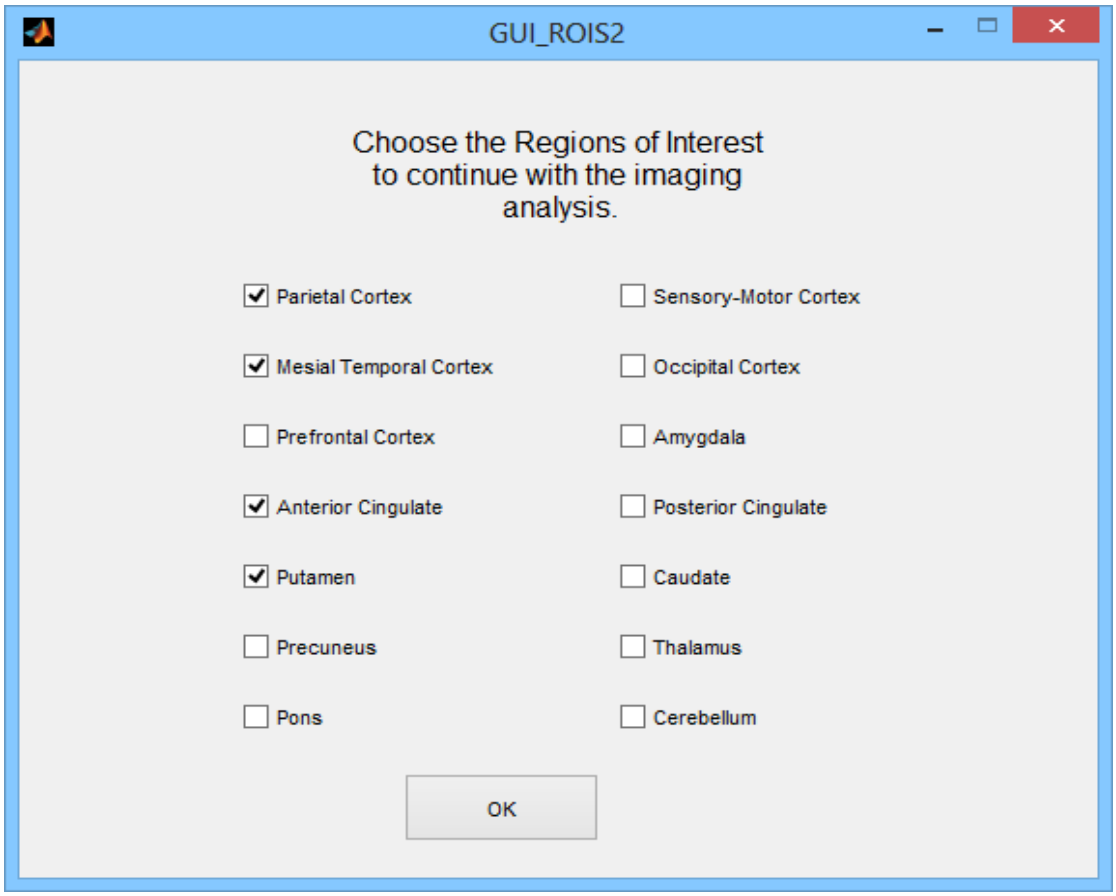


**Figure 5.8 - Interface to choose the ROIs to be registered to the reference space and used in PVC methods**

# CHAPTER 6

## DEVELOPMENT AND IMPLEMENTATION OF PVC METHODS – RESULTS

This chapter contains the results achieved with the implementation of the PVC methods in the pipeline as well as the respective discussion. The uncorrected data is also shown in order to spot the differences and the effective improvements comparing the images with and without the application of PVC. All the displayed images represent the same slice of the same brain, and the volumes were registered to the MR space for visualisation and analyses.

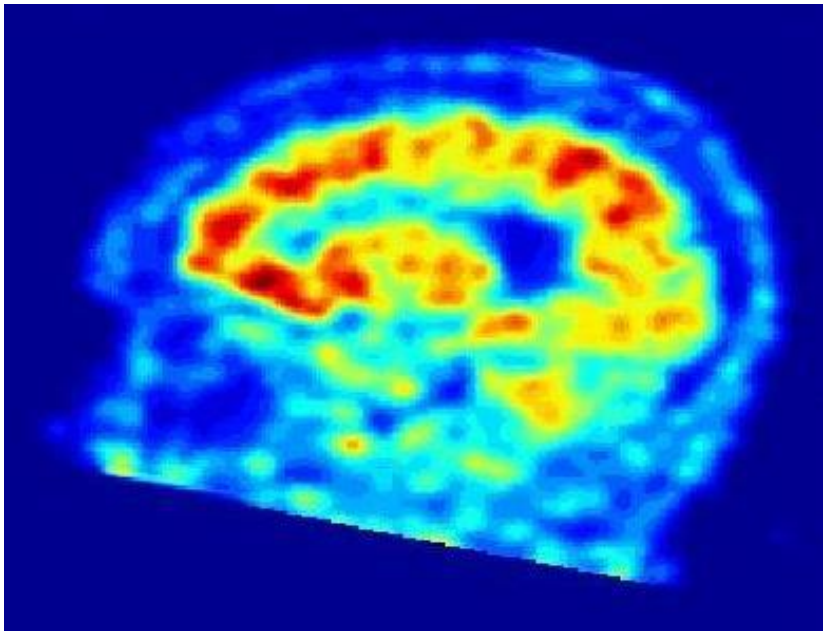

**Figure 6.1 - SUVr image with no correction**

This patient corresponds to an AD positive subject. As it is possible to observe, regions as frontal cortex, posterior cingulate and precuneus show an increased uptake of PiB. Contrasting with the information detailed on chapter 2, the higher the PiB uptake, the greater the amount of Aβ deposition on such regions, indicating an advanced state of the disease. The symptoms may be evident at this stage and PiB imaging plays an important role herein. It provides a clinical confirmation about the neurologic situation of the patient in terms of PiB uptake, which allows the neurologist to make the appropriate decisions relying on the treatment that can be applied.

## *6.1. Clean-up of results*

Particularly, in VC method the noise is amplified to great proportions and that is the reason why the process is stopped after a few iterations. In addition, some modifications were necessary to be applied in this method as well as in the other deconvolution techniques due to the great

amounts of noise that remained in the images after the processing has been concluded. It was verified, that the output was most of times generating some voxels with negative values, mainly in the lower boundaries of the head. In the PET context it is impossible to have negative activity so this was obviously the noise amplification taking place and in the end of the process all the negative values were changed by zero. The negative values were affecting the colour scale and the scans were difficult to be analysed. This difficulty was also increased because, like in RVC and RL, in the borders of the images, great amounts of noise were always being added to the images, as a result of the deblurring processes (Figures Figure 6.2, Figure 6.3, andFigure 6.4).

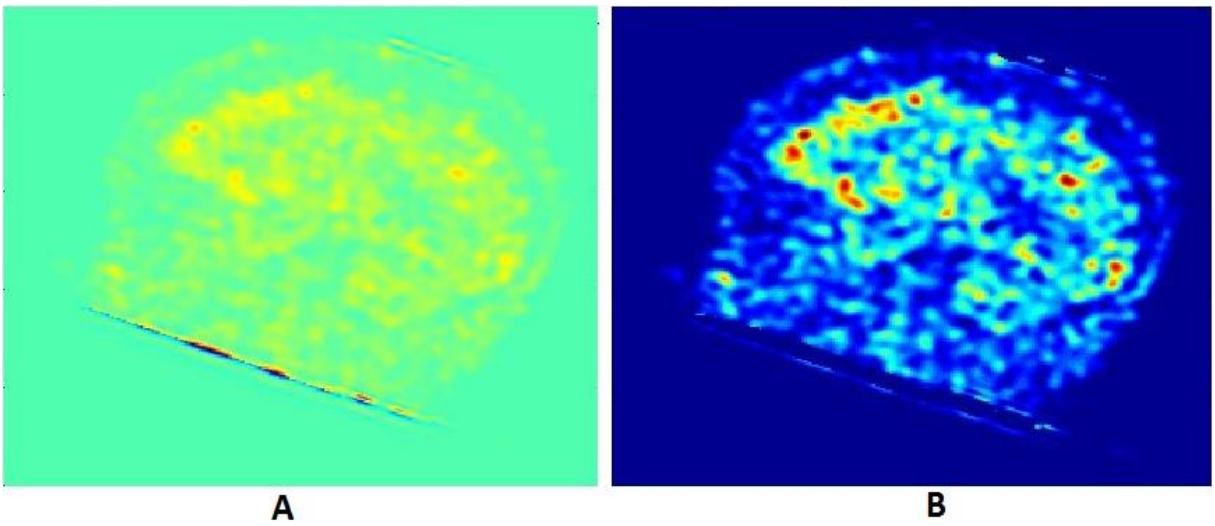


**Figure 6.2 - VC noise cleaning results comparison. A) Before cleaning; B) After cleaning**

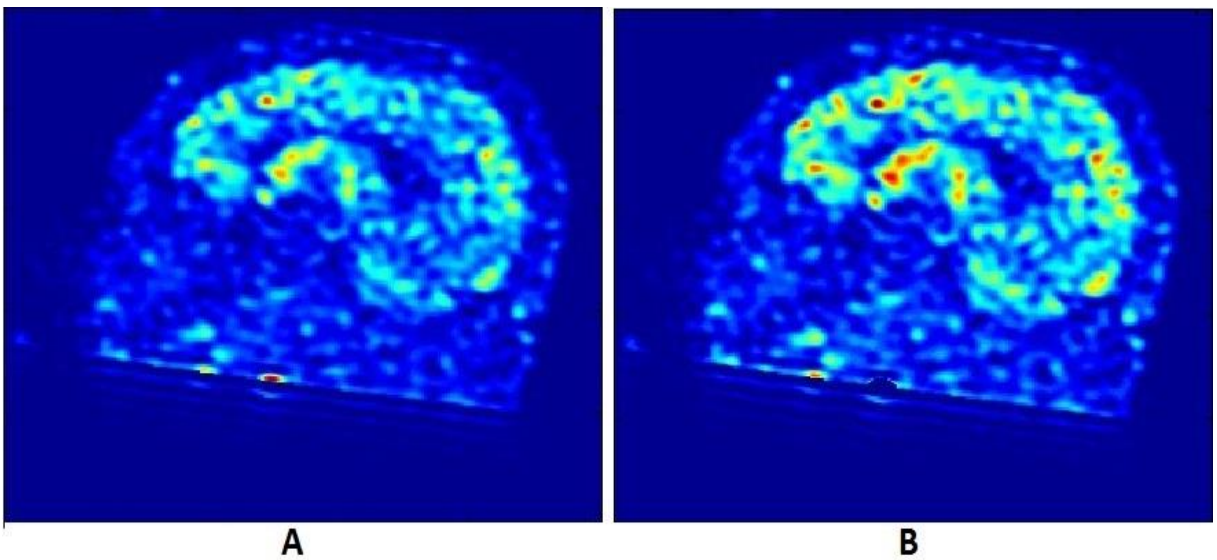


**Figure 6.3 - RVC noise cleaning results comparison. A) Before cleaning; B) After cleaning**

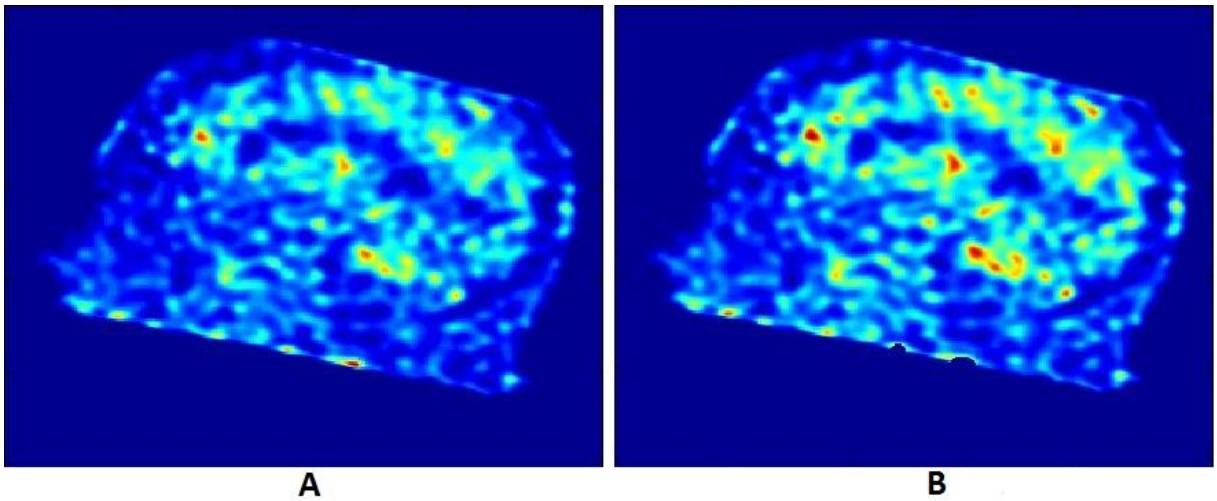


**Figure 6.4 - RL noise cleaning results comparison. A) Before cleaning; B) After cleaning**

The steps that leaded to the cleaning-up of the output are described in a few points:

- Image gradient calculation

In all the images this noise was being represented by sections where there were voxels with extremely high uptake values followed by voxels with extremely low uptake values, generating, thus, regions with a great gradient of uptake values. This effect was quite observable within the images and it was producing a region with a typical noise. The step described herein relies on the image gradient calculation. This is performed because through visual interpretation, it is expected a great gradient on this noise region. Once calculated the gradient, using MATLAB functions, the aim was to isolate the regions where the gradient was higher than the normal one, by defining a threshold (20% of the maximum gradient for VC and 75% for RVC and RL), and remove these regions from the images.

- Isolating the noise using MATLAB functions

After creating a binary image with the regions where the gradient was higher than the threshold, these sections were increased using the MATLAB function *imdilate*. In order to make it more robust, the area to be removed was dilated to assure that all the noisy area would be totally cleaned. This function dilates, by a factor of 4, the zone that corresponds to the increased gradient. After this, the noisy region was ready to be removed.

- Removing the noise from the images

Once isolated the region to be removed, in the form of a binary image, the PET image had to be filtered with that, in order to accomplish the cleaning process. Therefore, the binary image

was inverted: all the voxels whose value was zero were changed to ones and the same was done the other way around, transforming all the original ones in zeros. After this, the PET image that was going to be cleaned was multiplied by this transformed image. The final result is the original PET image without the region that corresponds to the previously identified noisy area.

The results of this cleaning task are showed below. The most evident differences correspond to VC correction since this is the method that contains a greater noise amplification.

## *6.2. PVC implementation - Results*

The results obtained with the PVC methods implementation are herein shown and discussed. Although the noise constraints that deblurring algorithms have on their mathematical framework, it was concluded that additional noise control needed to be made. This was a task that required time to be addressed and to find what could be made to improve the quality of the image without losing any important information from the image. This topic is properly discussed on the next section together with the results comparison.

Figure 6.5 was obtained using VC method, mathematically described on section 4.3.1. The convergence was achieved after 4 iterations and the differences between this image and the previous one (Figure 6.1) are notorious.

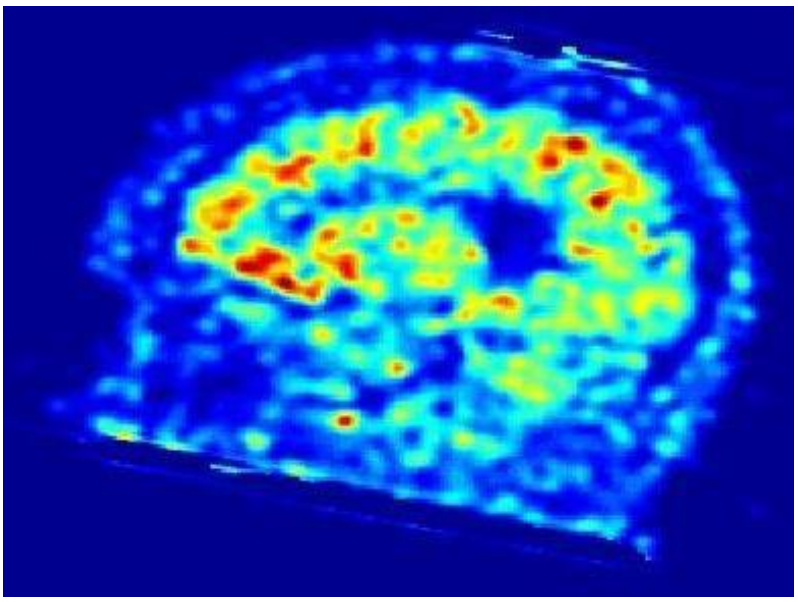

**Figure 6.5 - SUVr image corrected with VC method**

Figure 6.6 is obtained using RVC method and despite the similarities to Figure 6.5, this method is expected to be less noisy then VC since at the same time that the main deconvolution

is being performed an extra convolution is also being made [41]. This process assures a slower convergence and the noise stabilization [48], although the convergence criterion is the same. Nevertheless, the convergence was achieved after 54 iterations, taking longer than VC due to the greater complexity inherent to RVC method comparing to VC and also due to the softer convergence curve due to the reblurring step. In both methods the convergence factor $a$ was assumed as being 2, heuristically set from literature values [48].

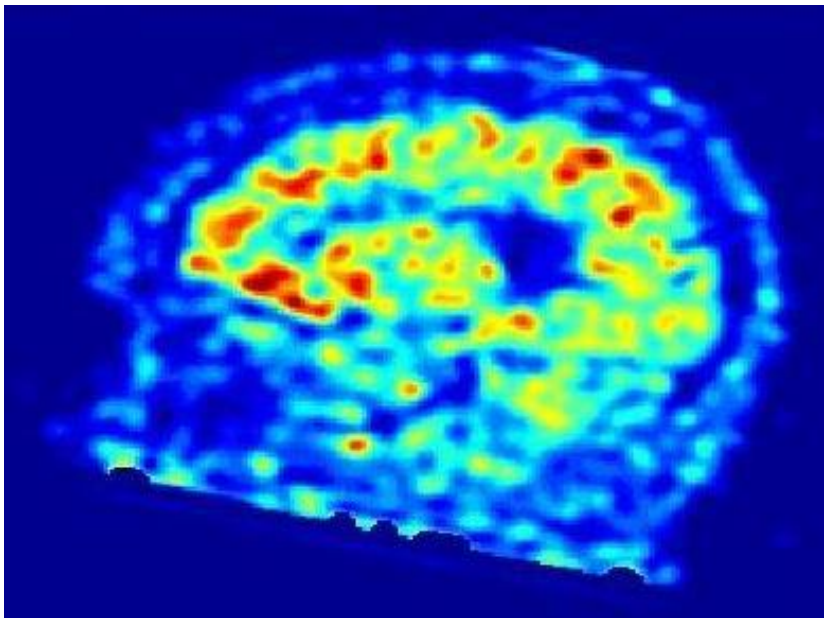

**Figure 6.6 - SUVr image corrected with RVC method**

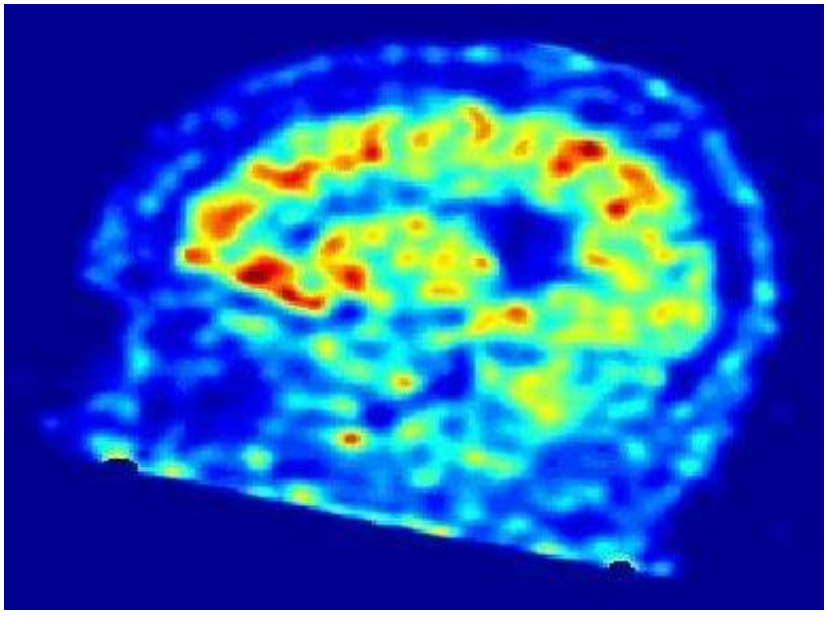

**Figure 6.7 - SUVr image corrected with RL method**

Apart from VC and RVC, RL is the other deblurring PVC method that has been implemented. Taking into account the algorithm performance, it is very similar to RVC method. The convergence was achieved after 49 iterations during approximately the same processing time. Figure 6.7 (above) shows the results of its implementation.

The last image-based PVC method is MG. This algorithm is not based on deblurring processes so there are no convergence criteria to be accomplished. MG method requires the segmented MRI scan to perform the correction and this is done just for grey matter. However, care is needed when using it because misregistration and/or misegmentation of the MRI scan frequently lead to errors of image correction. Figure 6.8 represents the correction achieved by MG method, whose performance was faster than RVC and RL methods. This can be explained based on the fact that the correction of the latter ones is done throughout all the brain, contrariwise to the one performed by MG, where it is just made over the grey matter as said before.

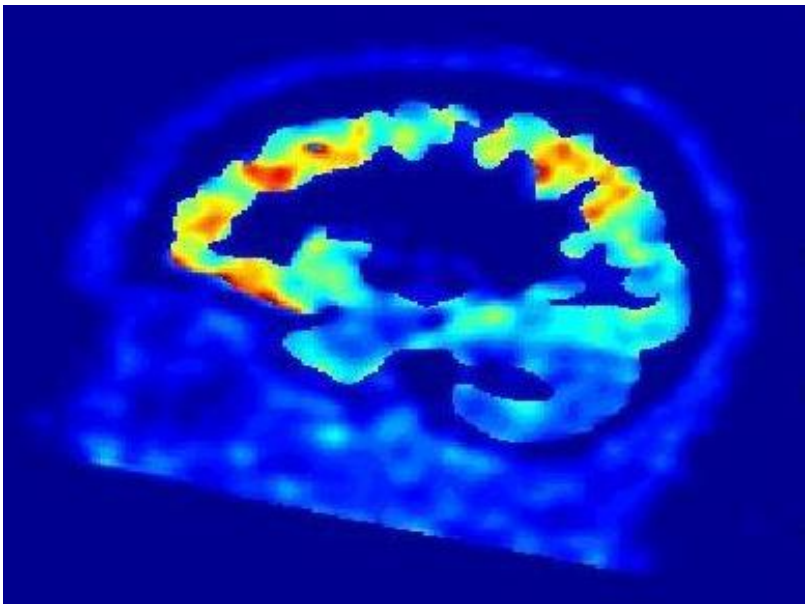

**Figure 6.8 - SUVr image corrected with MG**

By selecting the ROIs and applying the respective masks, it is possible to extract PiB uptake values from all the presented SUVr images. Having an image as input, Rousset method does not provide a corrected image as output, but rather the corrected uptake values for the grey matter of each selected ROI. The GTM matrix is also obtained in order to analyse the spill over effect among the ROIs. Table 6.1 contains the observed and corrected values for some ROIs extracted from the SUVr image shown on Figure 6.1.

**Table 6.1 - SUVr ROIs values (observed and corrected) and GTM obtained from Rousset PVC method**

| | Observed | | Putamen | Parietal | PC | Precuneus | Frontal | | Corrected |
|---|---|---|---|---|---|---|---|---|---|
| Putamen | 1,886 | | 0,514 | 0,000 | 0,000 | 0,000 | 0,002 | | 3,681 |
| Parietal | 1,566 | | 0,000 | 0,531 | 0,018 | 0,084 | 0,001 | | 2,865 |
| PC | 1,965 | | 0,000 | 0,018 | 0,608 | 0,356 | 0,005 | | 2,741 |
| Precuneus | 1,899 | | 0,000 | 0,091 | 0,418 | 0,605 | 0,001 | | 1,159 |
| Frontal | 1,700 | | 0,019 | 0,004 | 0,029 | 0,007 | 0,527 | | 4,076 |

On the table above, PC corresponds to Posterior Cingulate and Parietal and Frontal indicate the respective cortices (grey matter). Below, Table 6.2 presents a comparison among the same ROIs analysed on Table 6.1. The results are an average of the mean uptake value on each ROI on a group of 8 positive AD patients and the comparison is made over the five implemented PVC methods.

**Table 6.2 – Comparison of ROIs values among implemented PVC methods**

| | Rousset | MG | RL | RVC | VC |
|---|---|---|---|---|---|
| Parietal | 2,784 ± 0,292 | 2,012 ± 0,326 | 1,348 ± 0,182 | 1,351 ± 0,182 | 1,361 ± 0,183 |
| PC | 2,530 ± 0,414 | 2,245 ± 0,458 | 1,631 ± 0,179 | 1,632 ± 0,181 | 1,643 ± 0,181 |
| Precuneus | 1,236 ± 0,140 | 2,188 ± 0,439 | 1,717 ± 0,186 | 1,717 ± 0,190 | 1,729 ± 0,190 |
| Frontal | 3,571 ± 0,488 | 1,795 ± 0,339 | 1,494 ± 0,174 | 1,496 ± 0,177 | 1,506 ± 0,176 |
| Putamen | 3,504 ± 0,353 | 1,660 ± 0,255 | 1,728 ± 0,172 | 1,727 ± 0,172 | 1,738 ± 0,174 |

All these values were statistically tested in order to conclude about the significance of this comparison. The majority of them are indeed statistically significant with a p-value $< 0.05$ even after Bonferroni correction (not shown), as seen on Table 6.3. However, some values, mainly the

p-values between RVC and RL are not statistically significant and this fact can happen due to great similarity of the results provided by both methods. These values are already a great comparison in terms of output likelihood.

**Table 6.3 - Statistical Significance among all the PVC methods over the analysed ROIs**

| | Rousset vs MG | VC vs RVC | VC vs RL | RVC vs RL | MG vs RL | MG vs RVC | MG vs VC | Rousset vs RL | Rousset vs RVC | Rousset vs VC |
|---|---|---|---|---|---|---|---|---|---|---|
| Parietal | 9,60E-06 | 1,18E-04 | 7,41E-06 | 5,70E-02 | 1,13E-04 | 1,10E-04 | 1,29E-04 | 8,85E-07 | 8,33E-07 | 9,47E-07 |
| PC | 6,05E-03 | 7,36E-06 | 6,83E-05 | 2,82E-01 | 1,52E-03 | 1,47E-03 | 1,60E-03 | 9,67E-05 | 9,31E-05 | 9,99E-05 |
| Precuneus | 1,24E-03 | 1,97E-05 | 1,63E-04 | 8,37E-01 | 2,92E-03 | 2,72E-03 | 3,19E-03 | 6,99E-04 | 7,72E-04 | 6,47E-04 |
| Frontal | 4,91E-08 | 2,41E-06 | 4,40E-06 | 1,95E-01 | 4,32E-03 | 4,18E-03 | 5,09E-03 | 1,37E-06 | 1,31E-06 | 1,39E-06 |
| Putamen | 2,74E-09 | 7,16E-06 | 4,82E-05 | 3,31E-01 | 8,52E-02 | 8,75E-02 | 5,07E-02 | 4,57E-08 | 4,55E-08 | 4,55E-08 |

## *6.3. Comparison of PVC results*

It is clear that the implemented PVC methods provide distinct corrections on SUVr images. Among the five methods, deblurring algorithms are the ones that yield the most similar results, despite slight differences, having their mathematical frameworks based on deconvolution processes. As said before, this kind of methods increase the high frequency component of images resulting in excessive noise increments in the final output, so care is needed when using them.

In terms of quality of output, comparing VC and RVC, the corrected images show insignificant differences so the reason to choose RVC as the method to be applied is the lower levels of noise added to final image [48]. These algorithms are very similar, as is their implementations. The main disadvantage is that RVC is more time consuming, however, it is

compensated by the extra convolution that is used by the algorithm which tends to stabilize the noise production [49].

Comparing RVC to the other image restoration, RL, although very few, the visual differences are less evident. These algorithms contain distinct approaches based on noise models that are not the same, as explained before: while RVC correction assumes a noise process relying on a Gaussian distribution, RL correction is designed to correct the noise process that is described by a Poisson distribution [41]. Applied on the available data, both methods did not show relevant differences in terms of performance, except on the amount of iterations which was generally lower on the RL. The image quality is also very similar and the additive noise levels were almost undistinguishable. Researchers have already compared the quantification accuracy between RVC and RL, and when PVC is not applied [41]: in this study RVC quantitative performance was superior. This can be an indicator that RVC may be better than RL indeed. Thus, the choice of RVC instead of RL for PVC would be practicable and scientifically supported.

The other presented methods are MG and Rousset. On one hand, these methods have similarities because they perform their corrections taking into account both the tissue fraction and the PSF effect. On the other hand, the main difference between them is that MG provides an image as output and Rousset just give corrected values for the selected ROIs and the GTM matrix. As MG method relies on the assumption of tissue activity homogeneity, it is unable to compensate for PVEs between regions of the same tissue class. This fact can be assumed as a shortcoming of the method because in an AD subject the uptake in cortical regions often varies considerably [35]. The visual interpretation might be difficult because just the GM tissue is shown on the corrected images and this band frequently shows a shape variation on AD subjects, being significantly thin in some zones of the cortex [55]. Unlike the deblurring algorithms, MG needs the MRI scan and its segmentation to perform the method: this is a disadvantage when the scan is not available because it is impossible to use it. This method was, however, implemented because it has already been studied and well described on the literature [43] and the voxel-based correction would be interesting for comparisons among all the implemented PVC methods within the analysed data. MG has the advantage of considering the TFE. This effect is present because at the voxel level there may be regions where more than one tissue type may coexist. This frequently happens in the tissue boundaries as explained on section 4.1.2, and as a result, the activity of each tissue within a voxel (whose size is generally in the order of several mm per side [43]) will be expressed as the average of the total activity found on that space, leading to misunderstandings about the true activities – see Figure **4.3**. Nonetheless, the final output image

does not add significant value to the RVC corrected image, therefore, the latter still presents the best choice if the intention is the visual observation for diagnosis purposes.

Rousset can be compared to the other methods in terms of ROIs values because, as said before, it just provides corrected values and not an output image as the other methods. The considerations are almost the same as the ones taken by MG, with the exception of assuming region activity homogeneities instead of tissue activity homogeneity [42]. The main advantage of Rousset is that is possible to know how a specific region contributes to the activity observed in other regions on the uncorrected image, and its robustness assures that the noise amplification is very low during the correction processes. The method has shown to be suitable for dynamic PET studies and it may be very useful for quantitative methods since it can be used in order to provide corrected TACs although the aim here is to apply PVC techniques for semi-quantitative analysis. A study has been made comparing the Rousset and deblurring methods using grey matter maps (GMM) in order to assess if the correction performed by both methods would have the same results. The conclusions are detailed on the next section.

## *6.4. PVC using probabilistic grey matter maps*

VC, RVC and RL were compared to MG using probabilistic GMM. After performing the methods, the posterior cingulate region was assessed since it is known as an affected region in AD subjects. By using the probabilistic GMM it was expected that posterior cingulate uptake values were similar among the methods because this technique would add a kind of tissue fraction correction to deblurring approaches. The results have shown significant differences as expressed by Figure 6.9.

The values with red dots were achieved by multiplying the probabilistic GMM by the posterior cingulate mask and consequent application of the mask on the corrected SUVr images. This methodology was performed on a subset of 8 AD positive subjects and these values express the mean value for the posterior cingulate region PiB uptake. These values which are represented by the red dots were expected to be comparable to MG uptake values and if they were similar, a new method of using the deblurring algorithms together with the correction for the TFE would be achieved. The conclusions obtained from this study are that MG method may be overestimating SUVr values since the real activity is not known. In addition the usage of probabilistic GMM is not adding any additional useful information because the values with and without the multiplication of those are very similar.

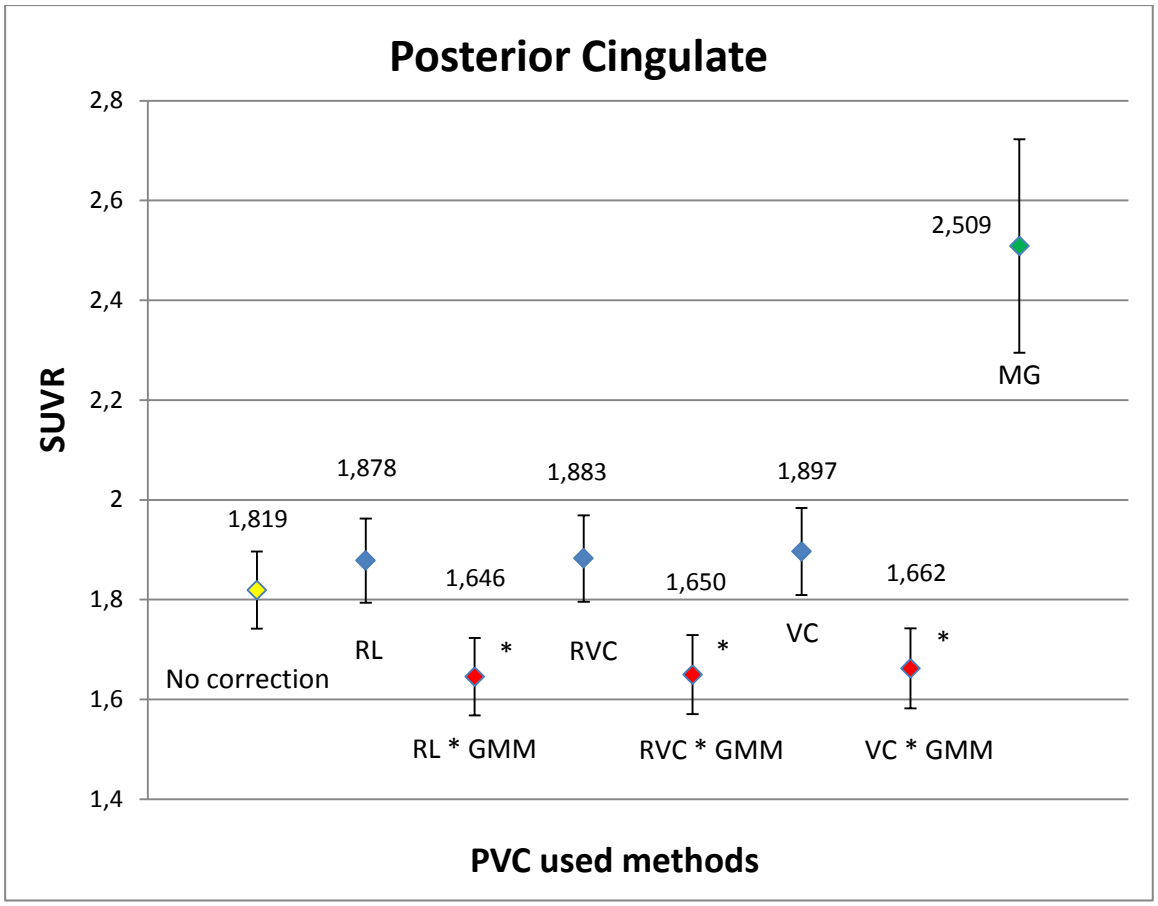


**Figure 6.9 - Comparison of MG and deblurring techniques by using probabilistic grey matter maps.**

(*) These values were statistically tested with a Paired T-Test. Each PVC + PVC*GMM pair has statistical significance with a p-value < 0,01

However, the available scans could not be enough to provide significant conclusions due to a few number of samples, so more scans would be necessary to provide a more complete analysis and perhaps results closer to what was expected. Future work is necessary for further conclusion about the discrepancy between the MG values and the ones from the deblurring methods. Nevertheless, the follow up studies should pay attention on the effective differences on the methodology between the deconvolution methods and MG because that may be one reason for such a discrepancy. The noise amplification is another detail that is inherent to the debluring algorithms mathematical framework [50]. The degree of amplification should be compared among those and MG, assessing signal to noise ratios of all the methods if necessary. After this step, proper conclusions can be drawn about the impact of the noise on the final outputs and if the methods are able to be compared.

# CHAPTER 7

## PATHOLOGIC SCANS CLASSIFICATION USING SUPPORT VECTOR MACHINES

## *7.1. Applying Machine Learning Methods for scans classification*

This last step has been done in order to achieve an automated confirmation about the state of dementia of the patient based on the PET scan. Linear classification has been used here with SVM, using a developed toolbox on MATLAB named PRoNTo (Pattern Recognition for Neuroimaging Toolbox) [67]. This type of classifier was chosen because it is robust and very used in neuroimaging classification, mostly in MRI studies.

The possible outputs for this classification were limited to "AD" or "no AD", and different input scenarios were assessed in trying to have the best results in terms of classification quality. The aim was compare all the image-based PVC methods (i.e. not Rousset) either registered to the standard space or registered to the MRI scan: as such, only scans from the subjects that had also undergone the MRI acquisition were used in this analysis.

The testing and training were done with cross validation. This procedure consists on analysing an initial data subset while the remaining data is then used to confirm and validate the initial analysis. There are several ways of performing the cross validation. Herein, leave-one-out was the chosen method. The algorithm uses a single observation from original sample as testing data, and the remaining observations as training data. This is repeated until each observation in the sample has been used once as the validation data [68].

The analysis was performed in 16 subjects (8 AD and 8 no AD). All these 16 scans were used multiple situations:

- VC, RVC, RL, MG and No Correction
- MNI and MRI
- SUV and SUVr

In total 20 different situations (modalities) are used having the four PVC methods and the images with no correction registered both to the MRI native space and to the standard space (MNI). The results of SVM classification are shown below on Table 7.1. These results are very useful to confirm the initial expectations, derived from visual interpretation of the outputs, about which PVC method would be the most valuable choice for general usage.

The Youden index was used to compare each modality in the classification procedures, by providing an indicator of the test performance [69]. It is a simple measure that is widely used by clinical researchers and statisticians, easy to apply due to the fact that it does not require additional information about prevalence rates, such as other classification indices [70].

## *7.2. Results of PiB scans classification*

Sensitivity and specificity values were visualized on PRoNTo toolbox and used to calculate the Youden index. The index is calculated by

$$Youden\ Index = Specificity + Sensitivity - 1 \qquad \textbf{Equation 7.1}$$

**Table 7.1 - Youden Indices for different modalities of PiB scans classification**

| | Sensitivity | Specificity | **Youden Index** |
|---|---|---|---|
| MNI_VC_SUV | 0,75 | 0,75 | **0,5** |
| MNI_VC_SUVr | 0,75 | 0,75 | **0,5** |
| MNI_RVC_SUV | 0,625 | 0,875 | **0,5** |
| MNI_RVC_SUVr | 0,75 | 0,75 | **0,5** |
| MNI_RL_SUV | 0,625 | 0,75 | **0,375** |
| MNI_RL_SUVr | 0,875 | 0,75 | **0,625** |
| MNI_MG_SUV | 0,875 | 0,75 | **0,625** |
| MNI_MG_SUVr | 0,875 | 0,875 | **0,75** |
| MNI_NoCorr_SUV | 0,5 | 0,75 | **0,25** |
| MNI_NoCorr_SUVr | 0,75 | 0,75 | **0,5** |
| MRI_VC_SUV | 0,75 | 0,75 | **0,5** |
| MRI_VC_SUVr | 0,625 | 0,875 | **0,5** |
| MRI_RVC_SUV | 0,75 | 0,75 | **0,5** |
| MRI_RVC_SUVr | 0,625 | 0,75 | **0,375** |
| MRI_RL_SUV | 0,75 | 0,75 | **0,5** |
| MRI_RL_SUVr | 0,75 | 0,75 | **0,5** |
| MRI_MG_SUV | 0,875 | 0,75 | **0,625** |
| MRI_MG_SUVr | 0,5 | 0,75 | **0,25** |
| MRI_NoCorr_SUV | 0,75 | 0,75 | **0,5** |
| MRI_NoCorr_SUVr | 0,75 | 0,625 | **0,375** |

From these results several conclusion can be achieved. First, the indices as a whole do not show a clear evidence that the classification algorithm is more accurate using the scans that are registered to the standard space rather than the MRI space: both reference spaces can apparently be used since the classifier performance was practically the same.

The second conclusion relied on the output format: SUV or SUVr. Although the used literature mention SUVr as the ideal output for PiB imaging and analysis, this fact was effectively tested by the used machine learning algorithm. Herein, there is a divergence on the classification results depending on the reference space that has been used. Most of the methods that had the scans registered to the MNI space achieved higher Youden indices for SUVr than for SUV. Contrariwise, when using MRI native space as the reference for the scans registrations, the results were the opposite, yielding higher Youden indices for SUV instead of SUVr. However, apart from VC, whose indices remained steady, all the other methods that used SUVr, including the non-corrected scans, achieved higher indices when registered to the standard space rather than to the MRI space, when comparing the same method but in different reference spaces. The same does not happen when this index comparison is made with SUV, which appears to be stable. This suggests an interaction effect between the choice of output space and type of quantity (SUV or SUVr). Therefore, based on the classification results no effective conclusions about the best output can be made but nonetheless, when using MNI as the reference space, the best choice is to choose SUVr as final output. According to the literature, as explained on chapter 3, SUVr is also suggested as the ideal final output. As a result, and since it is not possible to clearly demonstrate through classification that one output provides better results than the other one in terms of automatic AD diagnosis, SUVr is recommended to remain the standard.

There are further interactions between output space, quantity, and method. It would suffice to say that the conclusions, based on the classifier alone, critically depend on all factors involved. For instance, all three deblurring algorithms showed different performances depending on the reference space, with VC being the more robust to this choice. Using RVC or RL method, the classifier performed slightly better when using the MNI than MRI registration. The other image-based method, MG, was the one that achieved the highest score, using the SUVr images registered to the standard space.

There is no clear evidence as to the best PVC method to choose among all the ones tested here, provided by the classification results, with Richardson-Lucy and Müller-Gartner seen as contenders, the latter more robust to space selection. The absence of correction ("NoCorr" in Table 7.1) pointed out, however, through the poor scores that PVC should always be performed. Thus, this choice should be made based on the methods performance, regarding to what the user

wants to prioritize: either correct for both PSF and TFE effects if the MRI scan is available, obtaining a faster correction, but just for the grey matter, or using one of the deblurring algorithms, taking longer and just accounting for the PSF effect but obtaining a global image of the brain with no necessity of anatomy information.

The more scans available, the more efficient and realistic the classification results would be and perhaps different Youden indices would be achieved among all the PVC algorithms. It is important to underline that the lack of PiB-PET / MRI scan pairs is directly related to the classifier performance. This also created limitations on the validation process of the SVM classification. The cross validation scheme for classifier training purposes was the Leave One Out method, and the training data was the same that was used in the classification: there were not enough scans to use to different datasets, one for training and the other for the classification. Future work should include this kind of machine learning procedures in order to assess how the classification changes when using a higher amount of scans and different sets for training and classification. With this improvement, an evident discrepancy on the classification results is predictable, since all the methods provide different outputs as clearly seen through visual inspection.

# CHAPTER 8

## CONCLUSION

The prevalence of AD reflects the urgency of the active and permanent investigation in this field so as to understand more about this disease. This thesis focuses on the image processing analysis and how these processes can be improved for a more consistent and precise diagnosis. The early detection of the disease is a key factor and it has a great impact on the therapy steps the neurologist will take. Imaging techniques play a decisive role as they make it possible to assess *in vivo* the degree of severity of the disease, its progression and prognosis. PET is the gold standard of *in vivo* AD imaging as it allows for the detection of molecular changes that precede atrophy as seen e.g. in MRI. Notably, PiB-PET imaging provides valuable information about Aβ deposition on brain cortex, due to its great affinity with this protein, whose higher accumulation in certain regions of the brain is directly related with AD pathology. As such, PiB-PET is heavily studied in this field, seeking as much knowledge as possible about biological and functional responses of brain regions in the presence of PiB.

Two different approaches can be used to study the dynamics of this radiotracer in the brain: quantitative methods and semi-quantitative methods. Given the advantages of using the latter ones in the AD analysis, these are the focus of the developed pipeline. The developed method can, however, also be used with quantitative methods. Several enhancements were effectively achieved on the process of analysis, where some functions were improved, such as the frame realignment and image registration, and other features were added, like the possibility to extend the analysis to other radiotracers where the program can now load a new acquisition protocol if necessary, and the ability to choose the ROIs for extracting uptake values if a more detailed analysis is required.

Since these images are the ones used for the diagnosis, it was important to study how to improve the quality of the output for a more precise identification of the stage of the disease. Herein, PVEs are the major sources of error on PET images, thus the implementation of PVC methods was considered as being the key improvement of this pipeline. The research was addressed for already validated methods that could correct for TFE and PSF effects, since these originate PVEs on PET imaging. This task relied on the implementation of five methods, all of them with different methodologies.

On one hand, deblurring methods just account for the PSF effect and correct the whole of the input image, generating a global corrected image as final output. These output images have frequently great amounts of noise that is necessary to remove. As such, a practical image processing solution was applied so as to remove noise spikes, usually generated by these deconvolution processes. It is important to clarify that this task was essential to extract all the relevant information these images could provide. Thus, it is possible to conclude that the original

mathematical framework was not enough for obtaining acceptable images, even when considering noise amplification constraints. However, the image cleaning procedures that were posteriorly implemented assure that these images can indeed be used for AD diagnosis purposes. On the other hand, MG and Rousset are region-based PVC methods that need anatomic information through a segmented MRI scan. While the former method provides grey matter corrected images, the latter just gives ROI values as final output.

The reason for implementing all these methods was to verify which of them achieves the best results in the clinical setting. Some conclusions can be reached: first, if the desired final output is in image format, then RVC or RL method are the most suitable for usage since based on the analysis made during this work, these methods showed consistency on the quality of the images and the noise amplification was properly controlled, resulting on a great upgrading in terms of image correction comparing to the non-corrected images; second, if the user requires a precise and detailed region-based analysis, then the Rousset method is appropriate given its robustness and fast performance. The pipeline allows bringing both advantages together, using both Rousset and deblurring methods to obtain corrected ROIs uptake values as well as the corrected image, simultaneously.

One of the major limitations of this work is the fact that the true activity on the brain of the patient is not known. For that, it would be necessary the use of phantoms to precisely assess whether the computed activity in the images is indeed the real activity on the respective brain locations. If this was known, further conclusions could have been reached, specifically regarding how closer to the truth the PVC methods are, relative to the uncorrected image, and in addition to know which PVC method was providing the more realistic uptake values. This, however, is not critical for the scope of this thesis as all methods presented here have been previously validated using this approach.

The automatic diagnostic based on the disease likelihood was another goal of this thesis, which in turn could also provide some insight as to which PVC method was the best for diagnostic purposes. A machine learning algorithm, specifically SVM, was used in order to assess if it was possible to implement an automatic classifier that could provide the information about the probability of a given scan belonging to a positive (AD type) or negative PiB subject. Efforts were made for this purpose using all the implemented PVC methods and analysing which of them assured the best results in classification procedures. Unfortunately, the lack of combined PET and MRI scans for the same subject did not allow setting a conclusive output from here, mainly due to the influence of statistics. Nevertheless, all the conclusions related to the best choice for image registration space (standard (MNI) or native (MRI) space) and type of final

image (SUV or SUVr) obtained from this step are presented on section 7.2. It is expected that with a higher amount of scans, better results on pathologic scan classification could be achieved: therefore, a follow up study shall regard the improvement of this step.

As a general conclusion, it is important to mention that the majority of objectives proposed on the beginning of this work were accomplished. Furthermore, additional work on the scope of this thesis, more precisely the application of probabilistic grey matter maps on PVC deblurring methods, was developed in order to enrich the conclusions on this field and was presented on a biomedical engineering conference. In fact, a complete pipeline of analysis was created and it is ready for being used on clinical environment. This was the main goal of this thesis and, despite the future work that is necessary to improve some details, all the work performed on the pipeline optimization is considered to be extremely useful and has led to increase the clinical value of AD PET imaging in Coimbra.

# REFERENCES

[1] "Alzheimer Portugal." [Online]. Available: http://www.alzheimerportugal.org/scid/webAZprt/defaultArticleViewOne.asp?articleID=863&categoryID=956.

[2] B. Dubois, H. H. Feldman, C. Jacova, S. T. Dekosky, P. Barberger-Gateau, J. Cummings, A. Delacourte, D. Galasko, S. Gauthier, G. Jicha, K. Meguro, J. O'brien, F. Pasquier, P. Robert, M. Rossor, S. Salloway, Y. Stern, P. J. Visser, and P. Scheltens, "Research criteria for the diagnosis of Alzheimer's disease: revising the NINCDS-ADRDA criteria.," *Lancet neurology*, vol. 6, no. 8, pp. 734–46, Aug. 2007.

[3] "Alzheimer Europe," 2012. [Online]. Available: http://www.alzheimer-europe.org/.

[4] L. Hebert, P. Scherr, L. Beckett, M. Albert, D. Pilgrim, and M. Chown, "Age-specific incidence of Alzheimer's Disease in a community population," *Journal of the American Medical Association*, vol. 273, pp. 1354–9, 1995.

[5] "Alzheimer's Disease Progress Report 2011-2012.", U.S. Department of Health & Human Services, National Institutes of Health, National Institute of Aging

[6] L. P. Gwysher, "Care of Alzheimer's Patients: a Manual for Nursing Home Staff," 1985, pp. 25–27, American Health Care Association

[7] C. R. Jack, D. S. Knopman, W. J. Jagust, L. M. Shaw, P. S. Aisen, M. W. Weiner, R. C. Petersen, and J. Q. Trojanowski, "Hypothetical model of dynamic biomarkers of the Alzheimer's pathological cascade.," *Lancet neurology*, vol. 9, no. 1, pp. 119–28, Jan. 2010.

[8] D. W. Hwang, H. Youn, and D. S. Lee, "Molecular Imaging Using PET / MRI Particle," *The Open Nuclear Medicine Journal*, vol. 2, pp. 186–191, 2010.

[9] "Canada's national laboratory for particle and nuclear physics." [Online]. Available: http://www.triumf.ca/chemistry/radiochemistry-for-pet-imaging.

[10] S. Hatashita and H. Yamasaki, "Diagnosed Mild Cognitive Impairment Due to Alzheimer's Disease with PET Biomarkers of Beta Amyloid and Neuronal Dysfunction.," *PloS one*, vol. 8, no. 6, p. e66877, Jan. 2013.

[11] D. S. Knopman, "Diagnostic tests for Alzheimer diesease: FDG-PET imaging is a player in search of a role," *Neurology Clinical Practice*, pp. 151–153, 2012.

[12] P. Rosa-Neto and A. Leuzy, "Molecular Imaging of Alzheimer ' s Disease Using PET," *The Canadian Review of Alzheimer's Disease and Other Dementias*, pp. 18–25, 2008.

[13] K. a Johnson, N. C. Fox, R. a Sperling, and W. E. Klunk, "Brain imaging in Alzheimer disease.," *Cold Spring Harbor perspectives in medicine*, vol. 2, no. 4, p. a006213, Apr. 2012.

[14] J. R. Petrella, R. E. Coleman, and P. M. Doraiswamy, "State of the Art Radiology Neuroimaging and Early Diagnosis of Alzheimer Disease : A Look to the Future 1," pp. 315–336, 2003.

[15] J. R. Hesselink, "Basic Principles of MR Imaging.", Center for Functional MRI, Department of Radiology, School of Medicine, UC San Diego

[16] H. Panepucci and A. Tannús, "Magnetic Ressonance Imaging," São Carlos Physics Institute, University of São Paulo, Brasil, 1994.

[17] M. Brady, "Basics of MRI: MRI image formation," *Department of Engineering Science, Oxford University*, 2004. [Online]. Available: http://www.robots.ox.ac.uk/~jmb/lectures/medimanallecture1.pdf.

[18] C. R. Jack, "Mayo Clinic." [Online]. Available: http://www.mayo.edu/research/labs/aging-dementia-imaging/overview.

[19] C. A. Mathis, N. S. Mason, B. J. Lopresti, and W. E. Klunk, "Development of Positron Emission Tomography β-Amyloid Plaque Imaging Agents," vol. 42, no. 6, pp. 423–432, 2012.

[20] A. Forsberg, H. Engler, G. Blomquist, B. Långström, and A. Nordberg, "The use of PIB-PET as a dual pathological and functional biomarker in AD.," *Biochimica et biophysica acta*, vol. 1822, no. 3, pp. 380–5, Mar. 2012.

[21] J. C. Price, "PET Imaging of Brain Amyloid Using PIB," *The Dana Foundation*, 2004.

[22] B. J. Lopresti, W. E. Klunk, C. a Mathis, J. a Hoge, S. K. Ziolko, X. Lu, C. C. Meltzer, K. Schimmel, N. D. Tsopelas, S. T. DeKosky, and J. C. Price, "Simplified quantification of Pittsburgh Compound B amyloid imaging PET studies: a comparative analysis.," *Journal of nuclear medicine : official publication, Society of Nuclear Medicine*, vol. 46, no. 12, pp. 1959–72, Dec. 2005.

[23] S. M. Landau, C. Breault, A. D. Joshi, M. Pontecorvo, C. a Mathis, W. J. Jagust, and M. a Mintun, "Amyloid-β imaging with Pittsburgh compound B and florbetapir: comparing radiotracers and quantification methods.," *Journal of nuclear medicine : official publication, Society of Nuclear Medicine*, vol. 54, no. 1, pp. 70–7, Jan. 2013.

[24] W. E. Klunk, H. Engler, A. Nordberg, Y. Wang, G. Blomqvist, D. P. Holt, M. Bergstro, I. Savitcheva, M. L. Debnath, J. Barletta, J. C. Price, J. Sandell, B. J. Lopresti, A. Wall, P. Koivisto, G. Antoni, C. A. Mathis, and B. Långstro, "Imaging Brain Amyloid in Alzheimer ' s Disease with Pittsburgh Compound-B," *Annals of Neurology*, vol. 55, no. 3, pp. 306–319, 2004.

[25] M. D. Ikonomovic, W. E. Klunk, E. E. Abrahamson, C. a Mathis, J. C. Price, N. D. Tsopelas, B. J. Lopresti, S. Ziolko, W. Bi, W. R. Paljug, M. L. Debnath, C. E. Hope, B. a Isanski, R. L. Hamilton, and S. T. DeKosky, "Post-mortem correlates of in vivo PiB-PET amyloid imaging in a typical case of Alzheimer's disease.," *Brain : a journal of neurology*, vol. 131, no. Pt 6, pp. 1630–45, Jul. 2008.

[26] R. N. Gunn, A. A. Lammertsma, and V. J. Cunningham, "Parametric Imaging of Ligand-Receptor Binding in PET Using a Simplified Reference Region Model," *NeuroImage*, vol. 287, no. 6, pp. 279–287, 1997.

[27] H. Watabe, Y. Ikoma, Y. Kimura, M. Naganawa, and M. Shidahara, "PET kinetic analysis--compartmental model.," *Annals of nuclear medicine*, vol. 20, no. 9, pp. 583–8, Nov. 2006.

[28] J. Logan, "Graphical analysis of PET data applied to reversible and irreversible tracers.," *Nuclear medicine and biology*, vol. 27, no. 7, pp. 661–70, Oct. 2000.

[29] R. L. McNamee, S.-H. Yee, J. C. Price, W. E. Klunk, B. Rosario, L. Weissfeld, S. Ziolko, M. Berginc, B. Lopresti, S. Dekosky, and C. a Mathis, "Consideration of optimal time window for Pittsburgh compound B PET summed uptake measurements.," *Journal of nuclear medicine : official publication, Society of Nuclear Medicine*, vol. 50, no. 3, pp. 348–55, Mar. 2009.

[30] A. A. Lammertsma and S. P. Hume, "Simplified Reference Tissue Model for PET Receptor Studies," *NeuroImage*, vol. 158, no. 4, pp. 153–158, 1996.

[31] N. Tolboom, M. Yaqub, R. Boellaard, G. Luurtsema, A. D. Windhorst, P. Scheltens, A. a Lammertsma, and B. N. M. van Berckel, "Test-retest variability of quantitative [11C]PIB studies in Alzheimer's disease.," *European journal of nuclear medicine and molecular imaging*, vol. 36, no. 10, pp. 1629–38, Oct. 2009.

[32] S. Meikle, "Quantitative methods and factors affecting SUV calculation,", Department of PET & Nuclear Mecicine, Royal Prince Alfred Hospital, Sidney.

[33] I. Buvat, "SUV in PET : Silly or Smart Uptake Values," in *15th BHPA symposium 2010*, 2010, no. february.

[34] J. W. Keyes, "SUV: standard uptake or silly useless value?," *Journal of nuclear medicine : official publication, Society of Nuclear Medicine*, vol. 36, no. 10, pp. 1836–9, Oct. 1995.

[35] B. A. Thomas, K. Erlandsson, M. Modat, L. Thurfjell, R. Vandenberghe, S. Ourselin, and B. F. Hutton, "The importance of appropriate partial volume correction for PET quantification in Alzheimer's disease.," *European journal of nuclear medicine and molecular imaging*, vol. 38, no. 6, pp. 1104–19, Jun. 2011.

[36] I. a. Illán, J. M. Górriz, M. M. López, J. Ramírez, D. Salas-Gonzalez, F. Segovia, R. Chaves, and C. G. Puntonet, "Computer aided diagnosis of Alzheimer's disease using component based SVM," *Applied Soft Computing*, vol. 11, no. 2, pp. 2376–2382, Mar. 2011.

[37] A. Marquand, J. Rondina, J. Mourao-Miranda, V. Rocha-Rego, and V. Giampietro, *Pattern Recognition of Brain Image Data - PROBID*. 2010, p. 50.

[38] F. Pereira, T. Mitchell, and M. Botvinick, "Machine learning classifiers and fMRI: a tutorial overview.," *NeuroImage*, vol. 45, no. 1 Suppl, pp. S199–209, Mar. 2009.

[39] C. Campbell and Y. Ying, *Learning with Support Vector Machines*, vol. 5, no. 1. 2011, pp. 1–95.

[40] J. Mourão-Miranda, A. L. W. Bokde, C. Born, H. Hampel, and M. Stetter, "Classifying brain states and determining the discriminating activation patterns: Support Vector Machine on functional MRI data.," *NeuroImage*, vol. 28, no. 4, pp. 980–95, Dec. 2005.

[41] J. Tohka and A. Reilhac, "Deconvolution-based partial volume correction in Raclopride-PET and Monte Carlo comparison to MR-based method.," *NeuroImage*, vol. 39, no. 4, pp. 1570–84, Feb. 2008.

[42] O. G. Rousset, Y. Ma, and A. C. Evans, "Corrections for Partial Volume Effects in PET: Principle and Validation", *The journal of nuclear medicine,* vol. 39, no. 5, 1998.

[43] K. Erlandsson, I. Buvat, P. H. Pretorius, B. a Thomas, and B. F. Hutton, "A review of partial volume correction techniques for emission tomography and their applications in neurology, cardiology and oncology." *Physics in Medicine and Biology*, vol. 57, no. 21, pp. R119–R159, Dec. 2012.

[44] J. a D. Aston, V. J. Cunningham, M.-C. Asselin, A. Hammers, A. C. Evans, and R. N. Gunn, "Positron emission tomography partial volume correction: estimation and algorithms.," *Journal of cerebral blood flow and metabolism : official journal of the International Society of Cerebral Blood Flow and Metabolism*, vol. 22, no. 8, pp. 1019–34, Aug. 2002.

[45] "Philips - Imanalytics." [Online]. Available: http://www.imalytics.philips.com/sites/philipsimalytics/products/partial-volume-correction/partial-volume-correction.page.

[46] N. Boussion, C. Cheze Le Rest, M. Hatt, and D. Visvikis, "Incorporation of wavelet-based denoising in iterative deconvolution for partial volume correction in whole-body PET imaging.," *European journal of nuclear medicine and molecular imaging*, vol. 36, no. 7, pp. 1064–75, Jul. 2009.

[47] M. Soret, S. L. Bacharach, and I. Buvat, "Partial-volume effect in PET tumor imaging.," *Journal of nuclear medicine : official publication, Society of Nuclear Medicine*, vol. 48, no. 6, pp. 932–45, Jun. 2007.

[48] M. Allon, G. Debertrand, and M. Sleutjes, "Fast Deblurring Algorithms," pp. 1–25, [Online]. Available: http://citeseerx.ist.psu.edu/viewdoc/download;jsessionid=ABFAC879492FED5D46157603A109819A?doi=10.1.1.99.9392&rep=rep1&type=pdf

[49] J. Tohka and A. Reilhac, "A Monte Carlo study of deconvolution algorithms for partial volume correction in quantitative PET," *2006 IEEE Nuclear Science Symposium Conference Record*, vol. c, pp. 3339–3345, 2006.

[50] B.-K. Teo, Y. Seo, S. L. Bacharach, J. a Carrasquillo, S. K. Libutti, H. Shukla, B. H. Hasegawa, R. a Hawkins, and B. L. Franc, "Partial-volume correction in PET: validation of an iterative postreconstruction method with phantom and patient data.," *Journal of nuclear medicine : official publication, Society of Nuclear Medicine*, vol. 48, no. 5, pp. 802–10, May 2007.

[51] J. Biemond, R. L. Lagendijk, and R. M. Mersereau, "Iterative methods for image deblurring," *Proceedings of the IEEE*, vol. 78, no. 5, 1990.

[52] L. Åkesson, "Partial Volume Correction in PET / CT Master of Science Thesis in Medical Radiation Physics," University of Stockholm, 2008.

[53] M. Shidahara, C. Tsoumpas, A. Hammers, N. Boussion, D. Visvikis, T. Suhara, I. Kanno, and F. E. Turkheimer, "Functional and structural synergy for resolution recovery and partial volume correction in brain PET.," *NeuroImage*, vol. 44, no. 2, pp. 340–8, Jan. 2009.

[54] R. L. White, "Image Restoration Using the Damped Richardson-Lucy Method," in *The Restoration of HST Images and Spectra II*: proceedings of a workshop held at the Space Telescope Science Institute, Baltimore, Maryland, USA, 1994.

[55] H. W. Müller-Gärtner, J. M. Links, J. L. Prince, R. N. Bryan, E. McVeigh, J. P. Leal, C. Davatzikos, and J. J. Frost, "Measurement of radiotracer concentration in brain gray matter using positron emission tomography: MRI-based correction for partial volume effects.," *Journal of cerebral blood flow and metabolism : official journal of the International Society of Cerebral Blood Flow and Metabolism*, vol. 12, no. 4, pp. 571–83, Jul. 1992.

[56] C. C. Meltzer, P. E. Kinahan, P. J. Greer, T. E. Nichols, C. Comtat, M. N. Cantwell, M. P. Lin, and J. C. Price, "Comparative evaluation of MR-based partial-volume correction schemes for PET.," *Journal of nuclear medicine : official publication, Society of Nuclear Medicine*, vol. 40, no. 12, pp. 2053–65, Dec. 1999.

[57] D. Gutierrez, M.-L. Montandon, F. Assal, M. Allaoua, O. Ratib, K.-O. Lövblad, and H. Zaidi, "Anatomically guided voxel-based partial volume effect correction in brain PET: Impact of MRI segmentation.," *Computerized Medical Imaging and Graphics*, vol. 36, 2012.

[58] O. Rousset, A. Rahmim, A. Alavi, and H. Zaidi, "Partial Volume Correction Strategies in PET," *PET Clinics*, vol. 2, no. 2, pp. 235–249, Apr. 2007.

[59] J. M. S. Pereira, "Characterisation, Optimisation and Application of Voxel Based Morphometry in MRI Studies of Dementia," University of Cambridge, 2010.

[60] J. Ashburner and K. J. Friston, "Spatial Transformation of Images," in in *Human Brain Function*, R. S. J. Frackowiak, K. J. Friston, C. Frith, J. C. Mazziotta, and R. Dolan, Eds. American Press USA, 1997, pp. 43–58.

[61] J. Ashburner and K. J. Friston, "Unified segmentation.," *NeuroImage*, vol. 26, no. 3, pp. 839–51, Jul. 2005.

[62] R. Real and J. M. Vargas, "The Probabilistic Basis of Jaccard's Index of Similarity," *Systematic Biology*, vol. 45, no. 3, p. 380, Sep. 1996.

[63] S. Niwattanakul, J. Singthongchai, E. Naenudorn, and S. Wanapu, "Using of Jaccard Coefficient for Keywords Similarity," in *International MultiConference of Engineers and Computer Scientists, Hong Kong*, 2013, vol. I.

[64] J. M. Rasmussen, A. Lakatos, T. G. M. van Erp, F. Kruggel, D. B. Keator, J. T. Fallon, F. Macciardi, and S. G. Potkin, "Empirical derivation of the reference region for computing diagnostic sensitive $^{18}$fluorodeoxyglucose ratios in Alzheimer's disease based on the ADNI sample.," *Biochimica et biophysica acta*, vol. 1822, no. 3, pp. 457–66, Mar. 2012.

[65] G. S. Smith, S. L. Dewey, J. D. Brodie, J. Logan, S. A. Vitkun, P. Simkowitz, R. Schloesser, D. A. Alexoff, A. Hurley, T. Cooper, and N. D. Volkow, "Serotonergic Modulation of Dopamine Measured With [11C]Raclopride and PET in Normal Human Subjects," *The American Journal of Psychiatry*, vol. 154, no. April, pp. 490–496, 1997.

[66] U. M. H. Klumpers, D. J. Veltman, R. Boellaard, E. F. Comans, C. Zuketto, M. Yaqub, J. E. M. Mourik, M. Lubberink, W. J. G. Hoogendijk, and A. a Lammertsma, "Comparison of plasma input and reference tissue models for analysing [(11)C]flumazenil studies.," *Journal of cerebral blood flow and metabolism : official journal of the International Society of Cerebral Blood Flow and Metabolism*, vol. 28, no. 3, pp. 579–87, Mar. 2008.

[67] J. Mourao-Miranda, J. Schrouff, C. Phillips, M. J. Rosa, J. Rondina, A. Marquand, J. Ashburner, J. Richiardi, and C. Chu, "PRoNTo." [Online]. Available: http://www.mlnl.cs.ucl.ac.uk/pronto/index.html.

[68] E. Walter, "Pattern Classification in Neuroimaging: Support Vector Machines", Stanford University, 2009, [Online] Available: http://www.stanford.edu/~fumiko/psyc250_2009.files/Class4_SVM_psy250_walter_small.pd

f

[69] A. S. Glas, J. G. Lijmer, M. H. Prins, G. J. Bonsel, and P. M. M. Bossuyt, "The diagnostic odds ratio: a single indicator of test performance," *Journal of Clinical Epidemiology*, vol. 56, no. 11, pp. 1129–1135, Nov. 2003.

[70] N. Smits, "A note on Youden's J and its cost ratio." *BMC medical research methodology*, vol. 10, no. 1, p. 89, Jan. 2010.